DOI: 10.1002/((please add manuscript number))
Article type: Review

Scavenging Energy Sources Using Ferroelectric Materials

*Hongyu Li, Chris R. Bowen, and Ya Yang**

[*] Ms. H. Li, Prof. Y. Yang, CAS Center for Excellence in Nanoscience, Beijing Institute of Nanoenergy and Nanosystems, Chinese Academy of Sciences, Beijing, 101400, P. R. China.
E-mail: yayang@binn.cas.cn
Prof. C. R. Bowen Department of Mechanical Engineering, University of Bath, Bath BA27AK, UK
Ms. H. Li, Prof. Y. Yang, School of Nanoscience and Technology, University of Chinese Academy of Sciences, Beijing, 100049, P. R. China.
Prof. Y. Yang, Center on Nanoenergy Research, School of Physical Science and Technology, Guangxi University, Nanning 530004, P. R. China.

Keywords: ferroelectric, piezoelectric, pyroelectric, ferroelectric photovoltaic, nanogenerator

1. Introduction

With world-wide increases in energy consumption and a shortage of traditional energy resources, renewable and clean energy scavenging methods are arousing growing interest. In addition, the growth in the Internet of Things (IoT) requires a wide array of electronic devices and sensors that require multi-functionalization and miniaturization, which can greatly benefit from being autonomous, battery-free and self-powered. As a result, self-powered electronics must be able to scavenge energy from its surrounding environment efficiently. In this regard, *nanogenerators* have been examined as a form of miniature energy conversion device which can produce electric power from ambient mechanical motion, temperature changes or illumination.[1-3]

Ferroelectric materials are often applied in energy scavenging applications because of their large spontaneous polarization. Valasek discovered ferroelectricity in Rochelle

salt ($NaKC_4H_4O_6 \cdot 4H_2O$) in 1920 and ferroelectric materials have since been widely investigated.[4, 5] These fascinating materials have been used in a wide variety of applications such as phase shifters, frequency filters, oscillators, antenna, energy conversion, pressure sensors, hydrophones and actuators.[6-13] Ferroelectric materials possess a spontaneous polarization when they have a non-centrosymmetric phase structure below their Curie temperature (T_c). A distinctive feature of ferroelectric materials is that the orientation of the spontaneous polarization can be switched by the application of an external electric field. In addition, the polarization behaviour of ferroelectrics can be modified by a variety of methods, including controlling and engineering the material at the nano-scale, which have provoked significant academic and commercial interest.[14-22] There are over 700 ferroelectrics and the most studied materials are oxides and ferroelectric polymers. Two typical ferroelectric structures include the hydrogen-bonded structure and perovskite structure, as demonstrated in **Figure 1a** and 1b.[23, 24] $PbZrTiO_3$ (PZT) based ferroelectric materials display outstanding ferroelectric performance owing to the presence of a morphotropic phase boundary (MPB).[25-34] However the volatilization of lead (Pb) makes the long term use of lead containing materials deleterious to both human health and the environment.[35, 36] As a result, lead-free ferroelectric materials such as $BaTiO_3$ (BTO), $BiFeO_3$ (BFO), and $KNaNbO_3$ (KNN) have attracted the interest of researchers.[16, 37-42] In addition to the inorganic materials described above, polyvinylidene fluoride (PVDF) is a ferroelectric polymer, which is widely used in flexible devices such as wearable and foldable electronics.[43, 44] Ferroelectric materials are also often combined with other ferroelectric or non-ferroelectric materials to create *composites* and *multi-layered*

structures to optimize their properties and energy scavenging performance; for example, $K_{0.5}Na_{0.5}NbO_3$-$BaTiO_3$/PVDF composites and $PbZr_{0.53}Ti_{0.47}O_3/CoFe_2O_4$ multilayer architectures.[45, 46] These materials are being designed in the form of fine-scale nanostructures to obtain improved performance, for example, thin films, nanorods, nanowires, and porous ceramics.[47-50] In this regard, the energy scavenging performance of ferroelectric materials are strongly influenced by their remnant polarization, coercivity, dielectric constant and the electrode structure of any device.[51, 52]

Ferroelectric materials possess *piezoelectricity*, *pyroelectricity* and *ferroelectric photovoltaic* effects which correspondingly respond to a stimulus from mechanical, thermal and solar energy, respectively.[5, 53, 54] When a ferroelectric material is *poled* by the application of an external electric field, the spontaneous polarization is oriented in a single poling direction. The positive and negative bound charges will be restrained at the negative ends and positive ends of the polarization moments, respectively. The bound charges induce the depolarization field to keep the inside of the materials electrically neutral. And the free charges (or screening charges) accumulate to compensate the bound charges on the surface and keep the surface electrically neutral. Piezoelectric devices are able to convert mechanical vibration, air flow, human motion and biomechanical energy into electric power.[55-58] The application of mechanical forces changes the degree of polarization of the ferroelectrics and screening charges which have accumulated on two opposite surfaces of the ferroelectrics are free, which can drive a piezoelectric current in external circuit.[59] Ferroelectric materials can also convert low grade waste heat into electric energy through pyroelectric effects, due to a

similar change in polarization of the ferroelectric due to changes in temperature (dT/dt).[60] The ferroelectric photovoltaic effect can also produce charge and a voltage which is much larger than the bandgap of the material by absorbing solar energy, although the output photocurrent and the power conversion efficiency (PCE) is relatively low, and will be discussed in more detail later. The voltage output of a ferroelectric solar energy converter is proportional to the polarization and electrode spacing, rather than the bandgap of the applied material.[61-65] A common feature is that piezoelectricity, pyroelectricity and the ferroelectric photovoltaic effect all operate by influencing the polarization of a ferroelectric material. The similarity in the three mechanisms indicate that there is potential to couple the three effects to enhance the charge quantity and electric power from different energy resources simultaneously.[52, 56, 66, 67] As a result, delicately designed ferroelectric structures with a coupling of these energy harvesting effects will be discussed in this review.

A number of outstanding reviews on energy scavenging and the application of ferroelectric materials have been published, for example, Bowen *et al.* has summarized pyroelectric and piezoelectric energy harvesting devices[52] and Yuan *et al.* have provided a review on the applications of the ferroelectric photovoltaic effect.[61] Kenji Uchino updated his bestselling book, *Ferroelectric Devices*, in 2018 and the second edition provides a theoretical background and recent progress in novel ferroelectric materials and device design and manufacture.[68] J. F. Scott provided a historical review on the applications of ferroelectric materials in 2007.[5] However, the coupling of energy harvesting mechanisms and applications of ferroelectric materials have yet to be summarized systematically. As a result, this review focuses on the range of energy

scavenging effects of ferroelectric materials and novel nanogenerators based on these intriguing effects. This review will discuss the crystal structures of ferroelectrics and the mechanisms of ferroelectricity in detail, where piezoelectricity, pyroelectricity, the ferroelectric photovoltaic effect and the multi-effects coupling mechanisms of the ferroelectric materials will be explained in detail. The relevant definitions and equations are listed in this review, and we discuss the performance *figures-of-merit* and *power conversion efficiency* of ferroelectric based nanogenerators operating via different mechanisms to evaluate their performance. In addition, the differences between the common photovoltaic effect and ferroelectric photovoltaic effect are described with regards to solar energy scavenging applications. The fabrication methods used to create ferroelectric nanogenerators prepared by a variety of materials with diverse morphologies and nanostructures are described; these include PZT ceramic foams, BTO nanowire arrays, KNN nanorods, BFO bulk ceramics, and PVDF thin films. This review concludes with the working mechanisms of devices based on ferroelectric materials for different energy scavenging and a summary of recent high-performance energy harvesting nanogenerators. We conclude with the prospects of energy scavenging ferroelectric materials to stimulate further effort and inspiration in this growing research filed.

2. Ferroelectric effect

Ferroelectricity was initially reported by Valasek in 1920, which started to be applied in theoretical studies and engineering applications in 1943.[4, 5] Ferroelectric films were subsequently developed during 1960s-1970s.[69-76] In the late 1980s, ferroelectric films were integrated into semiconductor chips and applied to microsensors and micro-

electro-mechanical systems (MEMS) and devices.[77] The vital characteristic of ferroelectric materials is their switchable spontaneous polarization owing to their non-centrosymmetric crystalline structure.[53]

2.1. Structures and spontaneous polarization

2.1.1. Crystal structures and spontaneous polarization

Since their discovery, over 700 ferroelectric materials have been discovered. Potassium dihydrogen phosphate (KH_2PO_4) (KDP) is a typical hydrogen-bonded ferroelectric, [23, 78, 79] where the paraelectric KDP unit cell is shown in Figure 1a and the phosphates are bonded by H-bonds along the *a* and *b* axes. Another common ferroelectric crystal structure is the *perovskite* structure, which is shown in Figure 1b. The perovskite structure is denoted by ABX_3 (A, B are metal atoms, X is Oxygen atom or Halogen atom) where A is on the eight vertexes (blue balls), B is in the body center of unit cell, X is in the center of the six faces (red balls), and the green octahedrons are $[BX_6]$ octahedrons. [80] The spontaneous polarization of ferroelectrics originates from the inner structure, which can be divided into both electronic polarization and ionic polarization. Ionic polarization is produced from the vibration of the lattice structure, where the lattice vibration leads to a misalignment of the centers of positive charges and negative charges, which lead to the formation of *dipole moments*. Figure 1c shows a schematic of the spontaneous polarization of a perovskite $Pb(Mg_{1/3}Nb_{2/3})O_3$-$PbTiO_3$ in the rhombohedral phase along the [111] crystallographic direction. As shown in the diagram, the Mg/Nb/Ti ions in the B position move along eight isovalent [111] crystal orientations randomly and the movement of positive ions causes the centers of opposite charges to be misaligned and thereby produce dipole moments along the [111]

direction.[81] The spontaneous polarization of $BiFeO_3$ is also along the [111] direction due to the relative displacement of Bi, Fe, and O along the threefold axis.[82, 83] In contrast, the spontaneous polarization of $BaTiO_3$ is along [110] orientation, as a result of its tetragonal structure.[84]

2.1.2. Domain and domain wall motion

Before an external electric field is applied to a virgin ferroelectric material, there is no net polarization direction since dipoles are orientated in random directions. The neighbouring polarization dipoles in a micro- or nano-region of the material are in a common orientation and form a *ferroelectric domain*, where the *domain wall* is the interface between two contiguous domains. If the polarization orientations of two domains are perpendicular to each other, the domains are defined as 90° domains and the corresponding domain wall is a 90° domain wall. In addition, there are also 180°, 71°, and 109° domains, for example, which depend on the crystallographic structure and available polarization directions.[68, 85-87] The polarization direction of a ferroelectric can be switched by external electric field and a polarization-electric field (P-E) loop, shown in Figure 1d, demonstrates the processes of polarization reorientation and ferroelectric *hysteresis*, which can be ascribed to the interaction between domain wall motion and lattice defects. When the applied electric field is above the *coercive field* (E_c), the domains in the field orientation will grow through domain wall movement. The number and position of the defects randomly fluctuate and apply a randomly varying obstruction force to the domain wall. The obstruction force is therefore a function of distance, and the domain walls need to turn over one or more force peaks during their movement. When the electric field is removed, the domain wall

is unable to move over the force peak to return to the original position and it is possible to observe hysteresis phenomenon. If a reversed electric field in applied at the magnitude of the coercive field (E_c), the domain wall will be able to turn over the force peaks and return to the original position and the polarization will correspondingly decrease to zero; a further increase in the magnitude of the reversed electric field will lead to a net polarization in the reverse direction.[88-90]

Domain walls play an important role in energy harvesting of ferroelectric materials. The domain walls can be divided into 180° and non-180° domain walls, where the motion of non-180° domain walls can induce a dielectric and piezoelectric response, whereas 180° domain wall motion can only introduce dielectric response.[91] Xu *et al*. investigated the domain wall contribution to dielectric and piezoelectric performance of lead zirconate and titanate (PZT) films. They found that the *intrinsic* contribution of PZT thin films originates from individual domains, while the *extrinsic* contribution is from domain wall motion. [92] Pavel also proposed that the piezoelectric response of PZT film is proportional to the volume fraction of non-180° domain walls and this effect is speculated to be valid in many ferroelectric materials with a perovskite structure.

In addition to applied electric field, temperature can play a part in controlling domain structure and motion. For example, a high pyroelectric coefficient can be obtained at the phase transition point, where the temperature driving domain wall motion can be applied to control the extrinsic pyroelectric performance. [93] Karthik *et al*. examined the pyroelectric properties of epitaxial domain structures and came to a conclusion that temperature driven domain wall motion can improve the pyroelectric performance of PZT thin films under a state of tensile strain. [94] Defects also control domain motion.

For example, Yang Bai *at al.* investigated the pyroelectric and piezoelectric performance of (1-x)$KNbO_3$-x$BaNi_{1/2}Nb_{1/2}O_{3-\delta}$ (KBNNO), where oxygen vacancies and defect dipoles in pyroelectric materials are able to pin domain walls and reduce the polarization and further affect the pyroelectric and piezoelectric response.

Domains also contribute to the ferroelectric photovoltaic effect, which can be attributed to a bulk photovoltaic effect and a domain wall photovoltaic effect. The bulk photovoltaic effect is due to spatial inversion symmetry breaking of a polar lattice, while the domain wall photovoltaic effect originates from the spatial rotation of the polarization across domain walls. In addition, a charged domain wall can narrow the bandgap, while an uncharged domain wall is independent of the bandgap.[95] Matsuo *et al*. produced x$BaTiO_3$-(1-x)$BiFeO_3$ (x = 0.1, 0.2) with nano-scale domains by $BaTiO_3$ substitution in $BiFeO_3$ and confirmed that multi-domain $BiFeO_3$ possesses a better photovoltaic performance than their single domain counterpart.[96] Ying Shi The *et al*. explained the role of non-180° domain walls in enhancing the photovoltaic effect, where they observed a polarization change and potential steps at 71° and 109° domain walls, where the potential difference across the domain walls are able to separate charges to generate electron-hole pairs and reduce their recombination and strengthen the photovoltaic effect. Therefore, the potential across the domain walls can generate a drift and diffusion current: one side is the electron current and the other side is the hole current. When the direction of current flow is perpendicular to the domain wall, an above-bandgap photovoltage can be obtained and it was concluded that this mechanism is suitable to all ferroelectrics.[95] Bai *et al*. also verified the domain wall effect on the photovoltaic performance of $(K_{0.49}Na_{0.49}Ba_{0.02})(Nb_{0.99}Ni_{0.01})O_{2.995}$ (KNBNNO) and

showed that domain-light interactions can enhance the piezoelectric charge coefficient (d_{33}) of the material. The d_{33} of illuminated KNBNNO was 39 pC/N, which was 56% higher than that in a dark condition as a result of photo-stimulated domain switching. The short-circuit current, maximum output power and photovoltaic energy conversion efficiency of KNBNNO were all affected by the d_{33}, where a high d_{33} was obtained by a high net polarization and highly aligned domains. The application of a DC bias can also improve the domain order of ferroelectrics; therefore, it is possible to enhance the ferroelectric photovoltaic response by applying DC bias.[97] In conclusion, domain walls and domain wall motion both contribute to the energy harvesting performance of ferroelectric materials in response to mechanical, thermal and light stimuli. It is possible to enhance and control their dielectric, piezoelectric, pyroelectric and photovoltaic response by regulating the motion of domain walls using strain, defects, temperature, electric fields, light and the size of ferroelectric devices.

2.2. Ferroelectric phase transition and Curie temperature

The ferroelectric phase transition corresponds to the point at which the ferroelectric material transitions from a paraelectric state (with a acentrosymmetric structure) to a ferroelectric state (with a non-centrosymmetric structure); this is accompanied by a lattice distortion. The temperature dependent dielectric permittivity curves follow the *Curie-Weiss law*, where there is a polarization and dielectric anomaly around the ferroelectric phase transition temperature, which is called *Curie temperature* (T_c).[98-101] For example, cubic $BaTiO_3$ transforms to a tetragonal phase at a T_c ~120 °C, where the lattice parameter of cubic $BaTiO_3$ is a = 0.401 nm, while for the tetragonal phase of $BaTiO_3$ a = 0.399 nm, and c = 0.403 nm. Hence, the $BaTiO_3$ lattice structure can be

considred to be stretched along the c-axis during the ferroelectric phase transition. As displayed in **Figure 2a**, the dielectric permittivity of $K_{0.5}Na_{0.5}NbO_3$ ceramics is abnormally high at its T_c ~420 °C. the lower dielectric permittivity peak is ferroelectric to ferroelectric phase triansition. Figure 2b shows the relationship between temperature and dielectric constant of $0.6BaTiO_3@0.4SrTiO_3$ bulk ceramic at different frequencies, where we can observe a broadening of the dielectric peaks around 330 K. The Curie temperature decreases with an increase in frequency, which is a characteristic of a ferroelectric *relaxor*.[102] Figure 2c exhibits temperature-dependent Raman spectra of $KTa_{0.61}Nb_{0.39}O_3$ crystal. The Raman spectra show relaxor behaviours. The peaks of TO2, TO3 and TO4 do not exist in ferroelectric materials above T_c. But the TO2 and TO4 modes exist above T_c and until T_b (burns temperature) because of the polar nanoregions in the $KTa_{0.61}Nb_{0.39}O_3$ crystal caused by relaxor behaviour.[103]

2.3 Ferroelectric relaxor behaviours

Ferroelectric relaxor behaviours have aroused widely research interest in past years. Ferroelectric relaxors exhibit diffused phase transition and with the characteristics of broadened and suppressed dielectric Curie peaks, frequency-dispersive dielectric maxima and polar nano-regions. The normal ferroelectrics can be transformed into relaxor ferroelectrics by introducing non-equilibrium ions. For example, the ferroelectric phase can be transformed into relaxor state by heating above Curie temperature and depoling below a critical electric field.[104] And PVDF based polymers can obtain relaxor behaviours by introducing defects through high energy irradiation or further polymerization with chlorotrifluoroethylene or chlorofluoroethylene.[105] The ferroelectric relaxor polymers exhibit much higher dielectric permittivity than their

normal counterpart.[106] The interactions between the randomly distributing polar nano regions change the crystal structures of ferroelectric relaxors and strengthen the domain activity.[107] Therefore, ferroelectric relaxors exhibit better piezoelectric and dielectric properties. S. E. Park reported <001> oriented relaxor based rhombohedral $0.92Pb(Zn_{1/3}Nb_{2/3})O_3$-0.08PT crystal possess a ultrahigh piezoelectric coefficient of 2500 pm/V. The strain of 1.7% can be obtained at 120 kV/cm for $0.92Pb(Zn_{1/3}Nb_{2/3})O_3$-0.08PT because of the electric field induced relaxation rhombohedral-tetragonal phase transition.[108] Kutnjak reported that there is a critical point at the first-order paraelectric-ferroelectric phase transition where the piezoelectric coefficient is maximum. The polarization fluctuation near the point is large, which is responsible for the giant piezoelectric response. [109] Z. K. Xie *et al.* prepared $0.4Bi(Ni_{0.5}Zr_{0.5})O_3$-$0.6PbTiO_3$ and $0.38Bi(Ni_{0.5}Hf_{0.5})O_3$-$0.62PbTiO_3$ relaxor-ferroelectric films with a piezoelectric coefficient of 83.1 pm/V and 113±10 pm/V, respectively. The relaxor-ferroelectric films are predicted to be promising candidates for energy harvesting.[110] X. Y. Gao *et al.* synthesised relaxor ferroelectric $0.55Pb(Ni_{1/3}Nb_{2/3})O_3$-$0.135PbZrO_3$-$0.315PbTiO_3$ (PNN-PZT) ceramics. The relaxor performance generates large electroactivity, permittivity and strong domain activity, which further leads to the susceptibility to electric field and mechanical stress. Therefore, the PNN-PZT ceramics exhibit a high piezoelectricity and low coercivity. The piezoelectric stress coefficient, piezoelectric coefficient and maximum output current and maximum output power at the acceleration of 3.5g are 39.24 C/m^2, 1753 pm/V, 2.5 mA, 14 mW, respectively. The piezoelectric and energy harvesting performance are comparable to those of PMN-PT single crystal harvester.[111] The pyroelectric energy harvesting performance of relaxor

ferroelectrics can be improved when the relaxor-ferroelectric phase transition happens during the Olsen cycle. F. Y Lee *et al*. investigated the relaxor-ferroelectric phase transition temperature and pyroelectric energy conversion performance of $Pb_{1-x}La_x(Zr_{0.65}Ti_{0.35})_{1-x/4}O_3$ (x/65/35 PLZT) using Olsen cycle. The relaxor-ferroelectric phase transition temperature of 7/65/35 PLZT is about 180 ºC and the energy density is 1013.5±16.2 J l^{-1} per cycle at 0.026 Hz between 30 and 200 ºC and between 0.2 and 7 MV/m.[112] The relaxor behaviour of ferroelectric materials can be utilized to optimize their energy harvesting properties because of their unique domain structures and polarization behaviours.

3. Piezoelectric mechanical energy scavenging devices

3.1 Piezoelectric Effect

Piezoelectricity was discovered by Pierre and Jacques Curie in 1880s.[113, 114] The piezoelectric effect leads to the material generating electric charges when they are under mechanical stress and the number of the charges produced is proportional to the mechanical stress. Piezoelectric materials possess an asymmetric crystal structure. There are 32 groups of points and 21 are asymmetric. 20 of the asymmetric groups of points are piezoelectrics, except for the 432 group of points. [68] The relation of stress and electric displacement can be described by the equation:

$$D = dX \tag{1}$$

where D, d, X represents the dielectric displacement, piezoelectric constant and stress, respectively and d is the dielectric displacement per unit stress and indicates piezoelectric performance of piezoelectrics in terms of charge generation under a mechanical load. The piezoelectric coefficient d is anisotropic because of the crystal

structure and the properties of stress and is usually presented by d_{ij}. The first subscript of piezoelectric coefficient indicates the direction of electric displacement and 1, 2, 3 correspond to x, y, z axes, respectively. The second subscript represents the direction of the stress applied to the material. As an example, the d_{33} and d_{31} are the longitudinal and transverse piezoelectric coefficients respectively.

3.2. Performance Figure-of-Merit of Piezoelectric Nanogenerators

A piezoelectric nanogenerator is a form of self-powered electronic device and there are a variety of figures of merit to evaluate the piezoelectric performance. The piezoelectric strain constant d represents the ratio of electric displacement and applied stress of a piezoelectric, which means the materials with higher d possess larger electric displacement under the same stress and generate a large charge, and associated current when connected to an electrical load. The *piezoelectric voltage constant*, g, is defined by,

$$g = \frac{\partial E}{\partial X} = \frac{d}{\varepsilon_e} \tag{2}$$

where ε_e is the dielectric constant and materials with a high g will produce a high electric field (and associated voltage) under the same stress. The electric energy density produced under constant mechanical force is expressed by

$$U_{electric} = \frac{1}{2}\varepsilon_e E^2 = \frac{1}{2}\varepsilon_e (g \cdot \sigma)^2 = \frac{1}{2}(d \cdot g) \cdot \sigma^2 = \frac{1}{2}(d \cdot g) \cdot Y^2 \cdot \varepsilon_y{}^2 \tag{3}$$

where $U_{electric}$ represents electric energy density, σ is the applied stress, E is the induced electric field, Y represents Young's modulus, ε_y is the strain. Therefore, the figure of merit

$$FoM_{\sigma} = d \cdot g = \frac{d^2}{\varepsilon_e} \tag{4}$$

is related to the *electrical energy density for a given stress*, whereby materials with higher FoM_{σ} generate a higher electric energy density under the same stress.[115, 116] To evaluate the *electrical energy density for a given strain*, this can be expressed by

$$FoM_{\varepsilon y} = \frac{d^2 Y^2}{\varepsilon_e} \tag{5}$$

The electromechanical coupling factor k^2 is the ratio between the electrical energy stored in the device and the incoming mechanical energy. The value of k^2 indicates the energy conversion *efficiency* of piezoelectric nanogenerator.

$$k^2 = \frac{U_{electric}}{U_{mech}} = \frac{\frac{1}{2}(d \cdot g) \cdot (\varepsilon_y Y)^2}{\frac{1}{2}\varepsilon_y{}^2 Y} = \frac{d^2 Y}{\varepsilon_e} \tag{6}$$

where U_{mech} is the input mechanical energy The figure of merit k^2 can be applied to assess the efficiency of piezoelectric devices in terms of conversion of mechanical to electrical energy.[117]

The *maximum stored energy* of a piezoelectric device can be determined by the energy conversion efficiency and the mechanical energy that material can absorb without failure. A piezoelectric harvesting device can transfer an externally applied force into a mechanical strain energy. The maximum strain energy that the piezoelectrics can harvest is determined by the maximum strain and the Young's modulus of the piezoelectric materials. Thus, taking the maximum strain energy into consideration, the figure of merit can be written by

$$FoM_{\mathrm{m}} = k^2 \cdot u_y = \frac{d^2 (\varepsilon_{ym} Y)^2}{2\varepsilon_e} \tag{7}$$

where u_y represents the maximum strain energy, and ε_{ym} represents the maximum strain which the piezoelectric material can accommodate. Materials with a larger FoM_m exhibit larger maximum output electric energy without failure.[118, 119]

Electrical damping can affect the output performance of a piezoelectric energy harvester significantly. Therefore, the figure of merit in the off-resonance condition (constant force) can be expressed by

$$FoM_D = \left[\frac{d \times g}{tan\delta}\right]_{off} \tag{8}$$

where $tan\delta$ is dielectric loss tangent. In addition, when an oscillating force is applied on the piezoelectric element poled in the thickness dimension, the energy conversion efficiency is

$$\eta_{Pi} = \frac{1}{2}\frac{k^2}{1-k^2} \Big/ \left(\frac{1}{Q_m} + \frac{1}{2}\frac{k^2}{1-k^2}\right) \tag{9}$$

where Q_m represents the mechanical quality factor (which is the reverse of loss tangent). The energy conversion efficiency η_{pi} is only depended on Q_m and electromechanical coupling factor k^2.[114, 120-122] Therefore, the materials with high piezoelectric coefficient, Young's modulus, mechanical quality factor and low dielectric permittivity will possess high energy conversion efficiency. A low compliance is also required to reduce the damping. Therefore, a dimensionless figure of merit can also be expressed by

$$FoM_D = \left[\frac{d_{ij} \times g_{ij}}{tan\delta}\right]_{off} \times \left[\frac{k_{ij}^{\,2} \cdot Q_m}{s_{jj}^{\,E}}\right]_{on} \tag{10}$$

where s_{jj}^{E} is the compliance constant. The FoM_D has been used to evaluate the energy harvesting performance of some commercial piezoelectric ceramics and the validity has been proved.[123]

3.3. Ferroelectric materials for Piezoelectric Nanogenerators

Piezoelectric nanogenerators convert a variety of forms of mechanical energy into electric energy. The sources of mechanical energy include natural vibrations and movement, industrial vibrations, human motion and biomechanical motion. This section introduces ferroelectric materials with high piezoelectric performance and corresponding device architectures.

Ferroelectric materials with a morphotropic/polymorphic phase boundary (MPB/PPB) often exhibit an excellent piezoelectric response which is related to the polarization rotation and inter-ferroelectric phase transformation. The MPB/PPB indicates the coexistence of multiple phases or a transition driven by composition. PZT, KNN and PMN based ferroelectric materials at their MPB/PPB composition have been investigated in detail with regard to their improved properties at the phase boundary. Zhao *et al.* obtained $Pb(Mg_{1/3}Nb_{2/3})O_3$-$PbTiO_3$ single crystal with arombohedral/tetragonal morphotropic phase boundary that exhibited a high d_{33} ~ 1800 pC/N along the <001> and <011> directions.[124] Brajesh prepared $0.5Ba(Ti_{0.8}Zr_{0.2})O_3$-$0.5(Ba_{0.7}Ca_{0.3})TiO_3$ with a coexistence of both orthorhombic and rhombohedral phases and a high d_{33} ~ 570 pC/N.[125] A lead free KNN based ternary ceramic $0.96(K_{0.5}Na_{0.5})(Nb_{0.965}Sb_{0.035})O_3$-$0.01CaZrO_3$-$0.03(Bi_{0.5}K_{0.5})HfO_3$ with a MPB of rombohedral/tetragonal phases was fabricated by Li *et al.*, which exhibited an ultra-high d_{33} ~ 700 pC/N.[126] Yong Zhang *et al.* prepared Mn doped $0.92(Na_{0.5}Bi_{0.5})TiO_3$-

$0.04(K_{0.5}Bi_{0.5})TiO_3$-$0.04BaTiO_3$ ceramics with the coexistence of rhombohedral phase and tetragonal phase. The Mn doped sample achieved a FoM_σ of ~1790×10^{-15} m^2/N which is 1.5 times higher than that of undoped sample.[115] A piezoelectric vibration energy generator based on a PZT thin film with a MPB composition is displayed in **Figure 3a$_1$**. The flexible PZT film with a Zr/Ti ratio of 52/48 was prepared via a laser lift-off (LLO) process. The PZT film was spin-coated in the sapphire and then transferred onto a polyethylene terephthalate substrate by XeCl excimer laser irradiation. As illustrated in Figure 3a$_2$, the PZT thin film based flexible piezoelectric nanogenerator exhibits a high output voltage of ~200 V and short-circuit current of ~150 μA cm^{-2}, which is much higher than the previously reported energy generator.[127]

Flexible piezoelectric energy harvesting devices have aroused wide interest in recent years. Inorganic ferroelectric materials formed as composites with organic polymers such as PET, PVDF and their co-polymers have been reported. Kwonb *et al*. reported a $PbZr_{0.52}Ti_{0.48}O_3$ (PZT) ribbon based piezoelectric nanogenerator with PET substrate and semi-transparent graphene interdigitated electrode. The generated voltage outputs of the PZT based nanogenerator were ~1 V, 1.5 V, 2 V and the output current experienced a linear increase from 1 μA cm^{-2} to 2 μA cm^{-2} with applied forces of ~0.3 ± 0.02 kgf, 0.6 ± 0.02 kgf and 0.9 ± 0.02 kgf, respectively. [128] Chen *et al*. reported on P(VDF-TrFE)/BTO nanocomposite micropillar arrays for piezoelectric based energy harvesting. The flexible nanogenerator powered both a LCD screen and LED successfully and was able to operate as a highly sensitive self-powered sensor for detecting air pressure/flow.[129] Ju-Hyuck Lee *et al*. prepared a Highly flexible and stretchable transparent piezoelectric nanogenerators based on P(VDF-TrFE) as shown

in Figure 3b$_1$. The P(VDF-TrFE) thin film with flexible graphene electrode and stretchable PDMS template exhibits a 30 times higher output voltage than the normal nanogenerator at the same condition.[130]

The performance of ferroelectric inorganic/polymer flexible composites are also affected by their degree of inter-connectivity. The connectivity patterns can be divided into 0-3, 1-3, 2-2 and 3-3 according to the dimensionality of the active and matrix material, respectively. In this regard, the alignment of the active material in the flexible matrix is important to yield high *d* and *k* coefficients, and thereby achieve high performance figures of merit (Eqns X to Y). Yan *et al*. prepared a BTO nanofiber based nanogenerator with different degrees of alignment and compared their dielectric and piezoelectric performance. The highly aligned BTO nanofibers were prepared by an electrostatic spinning method were formed as a composite in a polydimethylsiloxane (PDMS) matrix. The BTO fibers were aligned randomly, horizontally and vertically in the matrix as shown in Figure 3c$_1$. The random fiber configuration can be considered as a 0-3 connection and the horizontal and vertical conditions reprsent a 1-3 connection. The results demonstrated that the nanogenerator with vertically aligned BTO nanofibers possessed the best dielectric and piezoelectric response, when compared with the other two connectivity conditions. The is due to the vertically aligned BTO being more sensitive to mechanical stress and possessing more efficient poling along the applied electric field direction. **Table 1** illustrates the range of piezoelectric mechanical energy harvesters formed from different ferroelectric materials and morphologies, which indicates that the morphologies of the materials have a strong influence on the output

performance of the piezoelectric mechanical energy scavenging devices.[27, 45, 48-50, 131-135]

4. Pyroelectric thermal energy scavenging devices

4.1. Pyroelectric Effect

The pyroelectric effect was scientifically analysed by Louis Lemery in 1717.[136] The micro mechanism of the pyroelectric effect is shown in **Figure 4a**, where the cations with positive charges are displaced relative to the centers of the negative charges and form dipole moments. The positions of the cations correspond to different quantised energy levels, which is demonstrated in Figure 4a. When the temperature of the lattice rises, the potential energy of the cations will increase and reaches new equilibrium positions. As consequence, the dipole moments formed by the misalignment of the centers of anions and cations will change. Taking the ABO_3 perovskite structure as an example in Figure 4a, the potential energy of the cation is increased because of the temperature rise and the cation will move from position **1** to position **2** of a higher energy level. The distance between the center of the anion and the cation is shortened, as shown in the schematic of the crystal lattice, which leads to a decrease of the dipole moment and a decrease in the overall spontaneous polarization. [137] As shown in Figure 4b, the spontaneous polarization dipoles are aligned between the electrodes of poling the ferroelectric using an external electric field. Bound and free charges will accumulate on the surface of the materials to balance the internal field caused by the highly aligned dipoles. When the temperature increases from T_0 to T, the dipole moments will lose their orientation and the polarization in the normal direction of the electrodes will decrease. Thus, if the pyroelectric device is in a short circuit conditions the net free

charges on the surface of the material will decrease by the transfer of charges as a pyroelectric current flows between the upper and lower surface via the external circuit.

4.2. Performance figures of merits of pyroelectric nanogenerator

The pyroelectric effect describes the relation between the spontaneous polarization (P) and the variation of temperature (ΔT). The ΔT can be presented by

$$\Delta T = \frac{W \times \Delta t}{c_E \times h} = \frac{W \times \Delta t}{c_p \times \rho \times h} \tag{11}$$

where W represents the power density of the thermal radiation on the pyroelectric element, Δt is the radiation time, c_E is the volume specific heat, c_p is the specific heat capacity, ρ represents the density, and h is the thickness of the material. The thermal energy for ΔT is

$$E_{thermal} = c_E \cdot A \cdot h \cdot \Delta T \tag{12}$$

where A represents the area of the electrodes. The pyroelectric coefficient can be described by

$$p = \frac{\partial P}{\partial T} \tag{13}$$

where p is the pyroelectric coefficient, P is the total polarization in the orientation perpendicular to the electrodes, and T is the temperature of pyroelectric device. Clearly, materials with higher p can generate a larger change in polarization, and therefore charge, for the same temperature change, where the charge generated is given by

$$\Delta Q = pA\Delta T = \left[\frac{p}{c_E}\right] \times \left[\frac{A}{h}\right] \times W \times \Delta t \tag{14}$$

where ΔQ is the change in charge on the surface, and A is the area of the electrode. Under a short circuit condition, the resulting pyroelectric current can be described by

$$i_p = \frac{\mathrm{d}Q}{\mathrm{d}t} = pA\frac{\mathrm{d}T}{\mathrm{d}t} = \left[\frac{p}{c_E}\right] \times \left[\frac{A}{T}\right] \times W \tag{15}$$

Therefore, the figure of merit related to the *current output* of the pyroelectric element is

$$F_i = \frac{p}{c_E} = \frac{p}{\rho \cdot c_p} \tag{16}$$

Therefore, materials with a higher F_i can generate a larger short circuit current from the same temperature fluctuation condition. The open circuit voltage of pyroelectric nanogenerator can be described by,

$$\Delta V = \frac{Q}{C} = \frac{p}{\varepsilon_{33}} h\Delta T = \left[\frac{p}{c_E \cdot \varepsilon_{33}}\right] \times W \times \Delta t \tag{17}$$

where ΔV represents the output voltage, and ε_{33} is the permittivity. Thus, the figure of merit related to the *output voltage* of the pyroelectric element is

$$F_V = \frac{p}{c_E \cdot \varepsilon_{33}} = \frac{p}{\rho \cdot c_p \cdot \varepsilon_{33}} \tag{18}$$

Therefore, materials with a higher F_V have higher voltage response under the same temperature variation. The electric energy stored in the pyroelectric device is

$$E_{electric} = \frac{1}{2} C(\Delta V)^2 = \frac{1}{2} \frac{p^2}{\varepsilon_{33}} Ah(\Delta T)^2 \tag{19}$$

where C represents the capacitance, and $E_{electric}$ is the induced electrical energy. Hence, the figure of merit reflecting the energy harvesting ability of pyroelectric generator in terms of *electrical energy* for a given change in temperature is

$$F_E = \frac{p^2}{\varepsilon_{33}} \tag{20}$$

The pyroelectric energy conversion coefficient is, which represents the *efficiency* is given by

$$\eta_{pyro} = \frac{E_{electric}}{E_{thermal}} = \frac{p^2 \Delta T}{2 c_E \varepsilon_{33}} \quad (21)$$

The pyroelectric energy conversion efficiency can be improved by enhancing the pyroelectric coefficient, lowering the volume specific heat and dielectric permittivity and broaden the temperature difference. Shishir Pandya *et al*. reported that the pyroelectric coefficient of $0.68Pb(Mg_{1/3}Nb_{2/3})O_3$-$0.32PbTiO_3$ thin film was improved to -550 μC m^{-2} K^{-1} and the dielectric permittivity was suppresses by 72% by applying electric field on the film. Then, the energy conversion efficiency was enhanced to 19% of Carnot cycle.[138] If we take the volume specific heat into account to consider the temperature change for a given thermal input, the stored energy and the figure of merit for energy scavenging can be modified as

$$E = \frac{1}{2}\left[\frac{\mathrm{p}^2}{\varepsilon_{33} \times \left(c_E^{\,2}\right)}\right] \cdot \left(\frac{A}{h}\right) \cdot (W \cdot \Delta t)^2 \quad (22)$$

$$F_E{}' = \frac{p^2}{\varepsilon_{33} \cdot c_E^{\,2}} \quad (23)$$

A lower volume specific means that there will be a larger temperature increase with the same incident thermal radiation. Therefore, materials with higher pyroelectric coefficient can produce larger polarization change and more charges at the same temperature fluctuation. In addition, as indicated by the pyroelectric figures of merit above, materials with lower dielectric constant can generate larger potential difference with the same level of surface charge.[139, 140] Zhang *et al*. proposed a figures of merits for evaluating the property of pyroelectric nanogenerators by measuring the *Q*-*V* curve of PVDF and PZT based pyroelectric nanogenerators. The energy harvested per cycle can be calculated according to the shadow area in **Figure 5a**$_1$ which can be expressed by

$$E_{cycle} = \int V \mathrm{d}Q \tag{24}$$

According to equation (14) and (17)

$$E_{cycle} = \int V \mathrm{d}Q = \frac{Q^2}{2C} = \frac{p^2 \cdot \Delta T}{4c_E \cdot \varepsilon_{33}} \cdot W \tag{25}$$

Therefore, the figure of merit for energy scavenging can be defined as

$$F_E'' = \frac{p^2}{c_E \cdot \varepsilon_{33}} \Delta T \tag{26}$$

F_E'' is termed the *universal energy scavenging standa*rd to assess the properties of pyroelectric energy harvesters. Charge-voltage (*Q-V)* diagrams of PZT and PVDF pyroelectric nanogenerators are illustrated in Figure 5 a_3 and a_4. The energy density of PZT is 2.76 times higher than that of PVDF and the result agrees with the value obtained from F_E'', which confirms the validity of F_E'' in assessing performance, The F_E'' of different materials are shown in Figure 5a_2 and F_E'' can be used to select pyroelectric materials and guide the device design.[141]

Zhang *et al*. examined the relationship between the fraction and alignment of the pores in porous PZT ceramic and its pyroelectric energy scavenging property using the figures of merit for pyroelectric nanogenerator. Figure 5b_1-b_4 illustrate the F_E', F_I, F_D and F_V of porous freeze-casting PZT ceramics with different connection modes and the porosity dependence of modelling and experimental results is listed. F_D is a modified form of Equation 23, where the loss is taken into consideration. The figure of merit for detectivity can be expressed by

$$F_D = \frac{p}{c_E \left(\varepsilon_{33} tan\delta\right)^{0.5}} \tag{27}$$

where *tanδ* is dielectric loss tangent. Both F_D and F_V increase with increasing porosity level and the F_D and F_V of the series-connected PZT are larger than those of the parallel-

connected PZT as a result of the lower dielectric permittivity. In contrast, the parallel connected materials have advantages in F_E' and F_I (F_i) over the series connected materials. This work confirmed the effectiveness of the above-mentioned figures of merit which can be applied to evaluate the performance of pyroelectric devices and guiding the device design.[142]

4.3 Pyroelectric cycles and energy conversion efficiency

Researchers proposed varieties of thermodynamic cycles to study and optimize the energy conversion performance of pyroelectric devices.

4.3.1 Carnot Cycle

As illustrated in Figure 4d, Carnot cycle is composite of 2 adiabatic steps (A→B, C→D) and 2 isothermal steps (B→C, D→A). In the first adiabatic process, the electric field and polarization are increased to the maximum value and the pyroelectric device is charged (A→B). Then the electric field is decreased to 0 isothermally (B→C). The followed adiabatic process is that the electric field is increased in inverse direction. Finally, the electric field undergoes isothermal decrease and returns to the original state (D→A). The energy conversion efficiency is defined as

$$\eta_{Carnot} = 1 - \frac{T_c}{T_h} \tag{28}$$

where T_h, T_c are the hot and cold temperatures, respectively. Carnot cycle is considered as the most efficient thermodynamic process for thermal energy conversion. Whereas, Carnot cycle is limited in practical application. And the efficiency of Carnot cycle is used for comparing with other cycles.[143, 144]

4.3.2 Olsen Cycle

Olsen *et al*. reported Olsen cycle in 1980s.[145] The 2 electrodes of the pyroelectric devices are respectively touched with a cold and hot source. As shown in Figure 4e, Olsen cycle possess two isothermal processes (A→B, C→D) and 2 constant electric field procedures (B→C, D→A). The out-of-plane electric field increases isothermally at the cold temperature (A→B), which followed by the increase of temperature at constant electric field (B→C). Then, the electric field is reduced at the hot temperature leading to a decrease of electric displacement (C→D). Finally, the temperature decreased to the initial value at the lower electric field (D→A).[52]

The area surrounded by A→B→C→D→A is corresponding the output electrical energy, which can be described by

$$N_D = \int E \mathrm{d}D \tag{29}$$

where N_D is the enclosed area, the electric field and electric displacement are represented by E and D, respectively. The output energy per cycle (δW_{cycle}) is

$$\delta W_{cycle} = -(T_h - T_c)\int_{E_A}^{E_B} P \mathrm{d}E \tag{30}$$

where P represents polarization, E_A, E_B are the electric field intensity at point A and point B, respectively. The input thermal energy is consisting of input thermal and electrical energy

$$Q_{\mathrm{in}} = c_E(T_h - T_c) + \int_{E_A}^{E_B} (P \cdot T_h) \mathrm{d}E \tag{31}$$

where Q_{in} is the total input energy, c_E is volume specific heat. Hence, the energy conversion efficiency is

$$\eta_{Olsen} = \frac{\int_{E_A}^{E_B} P\mathrm{d}E}{c_E + \frac{T_h}{T_h - T_c} + \int_{E_A}^{E_B} P\mathrm{d}E} \tag{32}$$

And the ratio of Olsen cycle energy conversion efficiency and that of Carnot cycle is

$$\frac{\eta_{Olsen}}{\eta_{Carnot}} = \frac{\int_{E_A}^{E_B} P \cdot T_h \mathrm{d}E}{c_E(T_h - T_c) + \int_{E_A}^{E_B} P \cdot T_h \mathrm{d}E} \tag{33}$$

The energy generated by electrocaloric effect Q_{ECE} is defined as

$$Q_{ECE} = T_h \int_{E_A}^{E_B} P\mathrm{d}E \tag{34}$$

Therefore, the ratio of the conversion efficiency of Olsen cycle energy and Carnot cycle can be expressed by

$$\frac{\eta_{Olsen}}{\eta_{Carnot}} = \frac{Q_{ECE}}{c_E(T_h - T_c) + Q_{ECE}} \tag{35}$$

Gaurav Vats *at al*. studied the energy scavenging applications of lead free pyroelectric materials: $K[(Nb_{0.90}Ta_{0.10})_{0.99}Mn_{0.01}]O_3$ (KNTM) and $0.5Ba(Zr_{0.2}Ti_{0.8})O_3$-$0.5(Ba_{0.7}Ca_{0.3})TiO_3$ (BZT-50BCT) by Olsen cycles. The maximum energy density of 629 mJ cm^{-3} (T_h = 160 °C, T_c = 120 °C, E_A = 0.1 MV/m, E_B = 5 MV/m) and 87 mJ cm^{-3} (T_h = 120 °C, T_c = 20 °C, E_A = 0.1 MV/m, E_B = 1 MV/m) is acquired for KNTM and BZT-50BCT, respectively.[146-150]

4.3.3 Brayton Cycle

Figure 4f illustrates the schematic of Brayton cycle, the enclosed cycle is composite of 2 isentropic processes (A→B, C→D) and 2 isoelectric processes (B→C, D→A). [151] The first step is charging the pyroelectric material in isentropic condition. Next, the pyroelectric material is heated at constant electric field, which followed by isentropic

charging. Finally, the pyroelectric material is cooled to the initial temperature isoelectrically. Compared with Olsen cycle, the isentropic processes displace the isothermal processes to improve practical operability. The energy conversion efficiency of Brayton cycle is

$$\eta_{Brayton} = 1 - e^{\frac{p\Delta E}{c_E}} \quad (36)$$

where $\Delta E = E_H - E_L$, p is pyroelectric coefficient. Brendan M. Hanrahan *et al*. investigated the pyroelectric energy transformation properties of PZT (Zr : Ti = 60: 40) thin film using Brayton cycle. A power density of 8 mW/cm^3 was obtained under the voltage of 5 V and excitation frequency of 0.2 Hz at ~60 °C.[143, 147]

4.4. Ferroelectric Materials for Pyroelectric Nanogenerators

Thirteen quadrillion British thermal units of energy is lost annually through waste heat by U.S. industry. [152] Waste heat is a by-product of vehicles and electric appliances such as refrigerators, air conditioning, data-servers, and high speed computers. Thermoelectric materials can convert spatial temperature gradients into electric energy by the Seebeck effect, while pyroelectric nanogenerators can convert temporal temperature gradients into electric energy. We have summarized recent work on pyroelectric nanogenerators in **Table 2**, where it can be seen that PZT based materials, lead free perovskite materials and triglycine sulphide (TGS) are potential materials for pyroelectric energy conversion. The FoMs such as F_E, F_E', F_V are also included in the table for comparison. In addition, ferroelectric materials are designed into particular microstructures, such as thin films, nanorods, porous structures and multi-layered structures to improve their output performance.[46, 47, 138, 142, 153-157]

Lead containing pyroelectric materials possess excellent pyroelectric output performance because their high polarization and phase transitions. Lead zirconate titanate, lead magnesium niobite and their compounds show morphotropic phase boundary (MPB) at certain compositions, which can enhance the polarization and pyroelectric response. Zhang *et al*. prepared PZT with 60% porosity which possesses an energy density of 1653 μJ/cm^3, where the porosity reduced the permittivity and heat capacity to increase the pyroelectric figures of merit. The FoM values were applied to evaluate the properties of the porous PZT ceramics. The p and F_I decreased with the increase of porosity, whereas, F_V, F_E' and F_D can be improved by the introduction of pores. [142] Lead magnesium niobite-lead titanate (PMN-PT) is a family of ferroelectric relaxor based compositions and the lattice structure of (1-x)PMN-xPT is related to the PT content. The PMN-PT is in a rhombohedral phase when x ≤ 0.31 and a tetragonal phase when x ≥ 0.35. When the PT content is x ~ 0.31 - 0.35, the rhombohedral, tetragonal and low-symmetry monoclinic phase coexist in PMN-PT materials and form a MPB. Pandya *et al*. prepared a 0.68Pb($Mg_{1/3}Nb_{2/3}$)O_3-0.32$PbTiO_3$ thin film based nanogenerator and investigated the pyroelectric performance of the 0.68PMN-0.32PT nanogenerator at different electric fields and temperatures by Olsen cycle (T_h = 115 °C, T_c = 25 °C, ΔE= 267 kV/cm). The F_E of the pyroelectric nanogenerator is enhanced by ~5 times while the dielectric constant is suppressed by ~70%. The peak value of power density and energy density of 0.68PMN-0.32PT based nanogenerator is 526 W cm^{-3} and 1.06J cm^{-3}, respectively.[138]

Lead free perovskite materials and their composites are also widely applied for thermal energy harvesting because they are non-toxic, environmentally friendly, and

their polarization and pyroelectric performance are comparable to lead containing materials. Lead free perovskite materials such as BTO, BST ($Ba_{1-x}Sr_xTiO_3$), KNN, BNT and their composites are often applied to fabricate pyroelectric nanogenerators. BST is a promising material for pyroelectric energy scavenging. BTO and STO ($SrTiO_3$) can form infinite solid solution and the physical properties of BST vary with the Sr content. BST possess low dielectric loss tangent, high breakdown field and slim hysteresis loops. Anoop R. Damodaran *et al.* reported a compositionally-graded BST film with polarization and strain gradients by pulse-laser deposition. They verified that the polarization gradients can induce large ferroelectric susceptibilities which is meaningful for energy scavenging performance. [158] A. lanculescu *et al.* investigated the pyroelectric performance of $BaSrTiO_3$ with different Sr content. The highest pyroelectric performance was obtained at 30% Sr because the Curie temperature of $Ba_{0.7}Sr_{0.3}TiO_3$ is close to room temperature.[159] Keshavmurthy *et al.* prepared porous $Ba_{0.85}Sr_{0.15}TiO_3$ ceramics with different porosity. The permittivity and volume specific heat decrease with porosity. Therefore, the figure of merits for current (F_i), voltage (F_V), detectivity (F_D) and energy harvesting (F_E, F_E') will increase with porosity. The F_D, F_E, and F_V of the porosity of 29.5% were increased by 19%, 61% and 210% compared with the dense counterpart.[160] Yang *et al.* fabricated $(1-x)K_{0.5}Na_{0.5}NbO_3$-$xBi_{0.5}Na_{0.5}ZrO_3$ (KNN-xBNZ) ceramics with a PPT region, which is achieved near room temperature by modification through doping. The pyroelectric coefficient of KNN-0.03BNZ is $p \sim 454.46\times10^{-4}$ $C/m^2\cdot K^1$ at the T_C and the figures of merit F_I, F_V, F_D, and F_E of KNN-0.03BNZ at room temperature are 1.83×10^{-9} m/V, 0.17 m^2/C, 0.34×10^{-4} $Pa^{-1/2}$, and 5.3 $J/m^3\cdot K$, respectively. [155] In addition to lead free perovskite

materials, triglycine sulphide (TGS) is a potential pyroelectric material for thermal energy harvesting and thermal sensing because of its high pyroelectric coefficient and low permittivity at room temperature. In addition, TGS shows high performance at room temperature due to its low ferroelectric phase transition temperature of 49 ºC. Ghane-Motlagh *et al*. prepared thin film containing oriented TGS nanorods whose phase transition temperature is 44 ºC and the corresponding pyroelectric coefficient p ~ 167 μC/m^2·K.[47]

PVDF is a ferroelectric polymer often used in flexible energy scavenging devices. Xue *et al*. prepared a PVDF thin film based wearable pyroelectric nanogenerator and a PVDF nanogenerator was installed on the N95 mask and harvesting energy via human respiration. The temperature variations arise from the temperature differences between the exhalant vapor and ambient temperature and the solidification heat of water vapor in the exhaled gas. When the environmental temperature is 5 ºC, the short-circuit current, open-circuit voltage and the maximum power under an external load of 50 MΩ are 2.5 μA, 42 V and 8.31 μW, respectively. The PVDF pyroelectric nanogenerator is able to charge a 10.0 μF capacitor to 1 V in 18s at 5 °C and drive both an LEDs and LCD.[154]

5. Solar energy scavenging devices

5.1. Ferroelectric Photovoltaic Effect

The conventional photovoltaic effect of semiconductors is based on the valence electrons absorbing photons to transfer into the conduction band, which leave a hole in the valence band. Incident photons should possess an energy exceeding the bandgap of semiconductors to offer sufficient energy for electron transition, and the photo

generating holes and electrons form hole-electron pairs. The charges are isolated by the built-in electric field of the P-N junction and the holes and electrons will accumulate at P region and N region, respectively, resulting in a photo-generated potential difference between the two ends of P-N junction. The build-in electric field is restricted into the depletion layer of the P-N junction, hence, the open-circuit voltage of the conventional optical photovoltaic effect is restricted by the bandgap of a semiconductor. In contrast, the built-in electric field in a ferroelectric photovoltaic material is due to its remnant polarization.[62, 161] As shown in Figure 4c, the built-in electric field exists in the entire ferroelectric material and charge separation is not restricted by the bandgap. Hence, the photovoltage of a ferroelectric material is abnormally high and can be higher than the bandgap.[66, 162, 163] The abnormal photovoltaic effect in $BaTiO_3$ and $LiNbO_3$ was reported in 1956 and 1969, respectively,[63] where the mechanism of the abnormal photovoltage effect has been discussed and is still not fully resolved. The integrated photovoltage can be considered as the photovoltage of the domains in a ferroelectric material connected in series. Ji *et al.* investigated the bulk photovoltaic effect of epitaxial ferroelectric $BiFeO_3$ thin films at visible wavelengths, where they verified that the orientation of the photocurrent and photovoltage can be flipped by reversing the polarization in two opposite directions of a $BiFeO_3$ thin film, which confirms the dominant effect of polarization on the ferroelectric photovoltaic effect. In addition, a negatively poled BFO film possesses a larger photovoltage, which indicates the existence of an internal bias field that is directed from the top electrode to the bottom electrode. The contribution of the photoresponse can be divided into two parts: the *ferroelectric polarization* and *internal field*, which can be expressed by

$$|V_p| = \frac{1}{2}(V_+ - V_-) \tag{37}$$

$$|V_{bi}| = \frac{1}{2}(V_+ + V_-) \tag{38}$$

where V_p is the voltage from the ferroelectric polarization, V_{bi} is the voltage due to the internal bias electric field, V_+ represents the open-circuit voltage obtained in a positive poling condition while V_- is that for a negative poling condition, respectively. According to the experimental results, the photovoltage from a switchable ferroelectric polarization is approximately two-fold higher than that from the irreversible internal field. The photocurrent is also related to the ferroelectric polarization, where the orientation of the photocurrent is antiparallel or perpendicular to the polarization direction. The steady photo current (J_s) depends on the symmetry of the materials and incident-light polarization. The total current is given by,

$$J = J_s + (\sigma_d + \sigma_{ph})E \tag{39}$$

where σ_d is the dark conductivity, σ_{ph} is the photoconductivity, and E is the applied electric field. The photoconductivity is given by,

$$\sigma_{ph} = eI_0\alpha\phi(\hbar\omega)^{-1}(\mu\tau)_{pv} \tag{40}$$

where I_0 is the light intensity, α represents the absorption coefficient, $\hbar\omega$ is the energy of incident photon, ϕ represents the quantum yield, μ is mobility and τ is the carriers' lifetime reliable for photoconductivity. [164] When J=0, the open-circuit voltage is

$$V_{oc} = E_{oc}d = \frac{J_s}{\sigma_d + \sigma_{ph}}d \tag{41}$$

where d represents the distance between the two electrodes.[163] Choi. reported on the reversible ferroelectric photovoltaic and diode effect of $BiFeO_3$, and the diode effect of

single-domain BFO crystal was investigated systematically where they observed that the forward orientation of the diode is always parallel to the ferroelectric polarization. Hence, the BFO diode orientation can be reversed by an applied electric field.[165]. Yi *et al.* further investigated the rectification effect of BFO single crystal and explained the underlying mechanisms. The switchable diode effect can be interpreted by Schottky-to-Ohmic contacts which is due to the alliance of polarization reversal and the electromigration of defects. In addition, the limitation of ferroelectric photovoltaic effect is that the photocurrent density is relatively small, typically in the order of nA cm^{-2}. [166] Efforts to improve the photoresponse of ferroelectric materials include using materials with a narrow bandgap and high breakdown strength and designing the micro- or nano-structured domains and domain walls.[167]

5.2. Performance Figure-of-Merit of Photodetectors

The photo energy conversion and detective performance can be evaluated by the figures of merit such as quantum efficiency (η), photoconductive gain (G), responsivity (R), power conversion efficiency (PCE) and detectivity (D^*). The quantum efficiency is the ratio of photoelectrons and incident photons, which can be described by

$$\eta(\lambda)=\frac{N\mathrm{h}\nu}{\Phi(\lambda)} \tag{42}$$

where $\eta(\lambda)$ represents the quantum efficiency when the wavelength of the incident light is λ. $\Phi(\lambda)$ represents the radiation power of the incident light. N is the number of photoelectrons, h represents Planck Constant ($h=6.62607015\times10^{-34}$ J·s), and ν is the frequency of the incident light. $\eta(\lambda)$ is the number of carriers generated by per incident photon in unit time.[168] The photoconductive gain G is the ratio between the quantity of charge carriers and absorbed photons

$$G=\frac{\Delta I/e}{PS/h\nu} \tag{43}$$

where ΔI is the difference between the photocurrent and the dark current, S is the active area, P represents the light intensity, e is the electronic charge, and hv is the energy of an incident photon.[169] The responsivity is used to assess the photoelectric energy conversion of photoelectric devices, which can be denoted by the formula

$$R=\frac{I_p}{P_{in}} \tag{44}$$

where I_p is the average output photocurrent and P_{in} is the incident light power. [170] The power conversion efficiency (*PCE*) represents the ratio of the input solar energy over the output electric energy, which can be expressed by

$$PCE=\frac{j_{PV}\cdot g}{\sigma_{PV}} \tag{36}$$

where j_{PV} is the steady-state current generated from a uniform illumination, g is the piezoelectric voltage tensor of the ferroelectric optical material, and σ_{PV} is the photoconductivity. Photoelectric devices with a higher *PCE* can generate more electric energy with same incident solar energy.[134] The detectivity D^* reflects the detectability for weak signals in noise environment. D^* is represented by

$$D^*=\frac{R}{\left(2e\cdot I_d/S\right)^{\frac{1}{2}}} \tag{45}$$

where I_d is dark current, R is responsivity.[171]

5.3. Ferroelectric Materials for Photovoltaic Devices

Ferroelectric photovoltaic devices are promising for photo detection and solar energy scavenging applications. Researchers have made significant effort to enhance the properties of the photovoltaic devices, in particular increasing the relatively small output current. The key to improving the properties of the devices are using ferroelectric materials with a narrow bandgap, designing micro- and nano-structured domain structures, and uniting the conventional photovoltaic effect with the ferroelectric photovoltaic effect. Examples of novel work reported in recent years are listed in **Table 3** and **Figure 6**, where the output performance and figure-of-merit of these photovoltaic devices are summarized in Table 3.[51, 162, 164, 172-175]

Inorganic ferroelectric materials with perovskite structure are often used in solar energy harvesting or photo detection. The bandgaps of typical perovskite materials are relatively wide (2.7-4 eV), which limits the photo absorption capability of perovskite materials and only 8-20 % of the solar spectrum can be absorbed. The wide bandgap of ABO_3 ferroelectric perovskite structure is due to the A-O and B-O bonds. The charges in the O 2p (valence band maximum) leap to the transition metal d states (conduction band minimum). Ma *et al.* fabricated an ITO/BTO/ITO photoelectric device, which is shown in Figure 6a_1. As shown in Figure 6a_2, a high photocurrent of ~400 nA and responsivity of 1.46×10^{-6} A/W are both obtained at 220 K. The reason for the performance enhancement at a low temperature are the activation of shallow traps and high polarization induced depolarization field, which suppresses the recombination of the photo-generated charges. In addition, the light-induced pyroelectric effect also enhanced the quantity of charges.[173]

BFO possess a narrow bandgap of 2.7 eV and is widely used to harvesting solar energy. For example, Zhao *et al.* reported an Ag/BFO/ITO photodetector with a two-dimensional structured electrode configuration. A schematic of the device is shown in Figure 6b$_1$ and, as illustrated in Figure 6b$_2$ and b$_3$, the peak values of the responsivity and photocurrent reached 6.56×10^{-4} A/W and 51.5 μA at 66.1 °C. [51] The photo energy of visible light is 1.64 - 3.19 eV, which represents 45~50% of the total solar energy. As a result, the bandgaps of photovoltaic materials need to be narrowed to absorb a broader range of visible light. The bandgap of BFO can be modified via doping and modulating the preparation conditions; for example, Quattropani *et al*. prepared epitaxial $BiFeCrO_6$ (BFCO) films on Nb-dope $SrTiO_3$ by Pulsed Laser Deposition. A schematic of the ITO/BFCO/Nb:STO device is illustrated in Figure 6c$_1$, where the authors fabricated a Cr doped double perovskite BFCO structure with a lowered bandgap of 1.9 eV. Figure 6c$_2$ shows the I-V curve of BFCO as the voltage sweeps from +8 V to -8 V. The short-circuit I_{sc} can be tuned from 0.9 to 2.2 μA and the average open-circuit voltage is 0.54 V.[176] Grinberg *et al.* investigated the visible-light-absorbing properties of a $[KNbO_3]_{1-x}[BaNi_{1/2}Nb_{1/2}O_{3-\delta}]_x$ (KNBNNO) solid solution prepared by solid-state methods. The band gap was narrowed by doping with two different transition-metal cations, where the band gaps of the KNBNNO composites are 1.1-2.0 eV with x = 0.1-0.4, which are lower than that of pure KNO (3.8 eV). The photoelectric performance of KNBNNO is also improved, where the photocurrent density of KNBNNO (40 nA cm^{-2}) is five times larger than that of the $PbLaZrTiO_3$ material (8 nA cm^{-2}).[162]

Organometal halide perovskites are composed of organic amine cations and BX_6 octahedron. The B is Pb or Sn, and X is usually a halide. Organic amine cations include

methylammonium (MA) $[(CH_3)NH_3]^+$, formamidinium (FA) $[NH_2(CH)NH_2]^+$, ethylammonium (EA) $[(C_2H_5)NH_3]^+$, guanidinium (GA) $[C(NH_2)_3]^+$), and imidazolium (IA) $[C_3N_2H_5]^+$).[177] These materials possesses a switchable polarization and narrow bandgap, which are advantageous for scavenging solar energy. Wang *et al.* reported on a biaxial trilayered hybrid perovskite molecular ferroelectric $EA_4Pb_3Br_{10}$. Figure 6d$_1$ shows the fabrication processed of a 3D $MAPbBr_3$ prototype into the 2D trilayered perovskite ferroelectric $EA_4Pb_3Br_{10}$. The $EA_4Pb_3Br_{10}$ material possesses a moderate optical band gap of 2.7 eV and is suitable for photovoltaic applications. As illustrated in Figure 6d$_2$, the V_{oc} and I_{sc} along a-axis is −0.49 V/+7.26 nA for the up-polarization state and +0.52 V/−6.36 nA for down-polarization state under 405 nm laser light.[178]

6. Coupled nanogenerators based on different physical effects

We have seen that ferroelectric materials are able to possess the piezoelectric effect, pyroelectric effect and photovoltaic effect simultaneously. These mechanisms are all strongly related to the polarization of a ferroelectric material. In addition, mechanical vibrations, temperature fluctuations and illumination often coexist in ambient environment. Therefore, the ability to couple the piezoelectric, pyroelectric and photovoltaic effects into a single-structured energy conversion device is an intriguing way to harvest different forms of energy synchronously. The coupling principles can also be used to fabricate multifunctional sensors. In this section, we introduce *hybrid* nanogenerators and sensors that couple the different effects. The photovoltaic performance of ferroelectric materials can be improved by inducing temperature and mechanical variations corresponding to pyroelectric and piezoelectric effects, respectively.

Ji *et al*. fabricated a BTO based nanogenerator that coupled piezo-pyro-photoelectric effects to increase the output signals of the energy harvesting device. A schematic of the device is illustrated in **Figure 7a$_1$** and Figure 7a$_2$ shows that the peak and stable currents under ‘‘light + vibration’’ are clearly higher than those under only ‘‘light’’ or ‘‘vibration’’ alone. Figure 7a$_3$ presents the charging performance of the nanogenerator, where the best charging performance was obtained under the condition of ‘‘light + vibration + wind’’. The results verified the multi-effect coupled strengthening effect. The application of vibration and wind to a photovoltaic device can enhance the charging performance. Since vibration and wind can enhance the polarization and depolarization field in the device by a stress or temperature decrease, the improved depolarization field can promote the separation of the light induced carriers.[67] Wang *et al*. examined a one-structure-based hybridized nanogenerator which coupled the piezoelectric and pyroelectric effects. As shown in Figure 7b$_1$, the hybridized nanogenerator consists of a PVDF nanowires-PDMS composite film and a polarized PVDF film. PVDF possess multi-physical properties and can output electric signals due to a stretching strain (piezoelectric) or heating (pyroelectric). The output signals of the device measured at a diverse range of conditions are demonstrated in Figure 7b$_2$ an b$_3$, where the hybridized nanogenerator possess better output performance than the individual counterpart. [179]

Pyroelectric, piezoelectric and triboelectric effects can work simultaneously to scavenging energy from temperature, mechanical and friction signals. Zhang *et al*. prepared a one-structure-based nanogenerator that coupled piezo-tribo-pyro-photoelectric effects. The one-structured-based nanogenerator consisted of a PZT bulk as pyroelectric, piezoelectric and photovoltaic active material, polyamide (nylon) as

flexible vibration layer. Figure 7c_2 and c_3 show that the peak current/voltage and platform voltage of the effects coupled nanogenerator is 5 μA/80 V and 50 V. [181] The photovoltaic effect leads to a high voltage platform, while the pyroelectric effect contributes to a voltage peak and the triboelectric effect promotes the output current. Therefore, the piezo-tribo-pyro-photoelectric nanogenerator exhibited a large output current and voltage simultaneously as a result of the coupling of different individual units. The hybrid energy conversion device can also operate as a multi-effect sensor to detect temperature, mechanical and other signals. Song *et al*. reported a temperature and pressure sensing device coupling piezoelectric and pyroelectric effects. Figure 7d_1 shows an image of the flexible device fabricated with BTO ceramic plates and PDMS. The BTO exhibits superior pyroelectric and piezoelectric performance and sensitivity to temperature and strain, where there is a synergetic combination of the pyroelectric and piezoelectric output. The output voltages shown in Figure 7d_2 and d_3 demonstrate that the multi-functional sensor can harvest temperature and pressure changes simultaneously without interference and can be applied as a flexible temperature and pressure detector for human finger touching such as password lock and keyboard.[180]

In conclusion, the coupling of multiple-effects can be achieved using a ferroelectric material which respond to a range of stimuli and integrating ferroelectric materials with different effects into a one-structured device. The research mentioned above confirm the effectiveness of the multi-effect coupled for enhancing the energy scavenging performance of nanogenerators. [181]

7. Summary and prospects

This review systematically introduces the energy scavenging mechanisms, performance and current progress of ferroelectric materials based nanogenerators. The piezoelectric, pyroelectric and photovoltaic nanogenerators for mechanical, thermal and solar energy scavenging are all illustrated in detail in the review. Table 1 - Table 3 demonstrate the recent reported ferroelectric nanogenerators which cover a wide range of ferroelectric materials including inorganic perovskite materials, ferroelectric polymers and ferroelectric composites with different geometrical morphology such as bulk ceramic, nanorods, nanowire arrays, thin films and multi-layered structures. The parameters and figures of merit used for evaluating the energy conversion performance of the ferroelectric nanogenerators are also summarized and factors affecting the output performance of the energy scavenging devices are summarised. The working mechanisms of the nanogenerators are all connected with the polarization and domain wall configuration of the ferroelectrics. These factors provide guidance on the selection of ferroelectric materials and design of device configurations.

Wearable and self-powered devices based on ferroelectric materials are the subject of increasing interest in recent years. As mentioned above, flexible ferroelectric materials are often PVDF based ferroelectric polymers or an inorganic ferroelectric active material formed as a composite in a flexible polymer matrix. As demonstrated in **Figure 8**, wearable devices based on the piezoelectric effect can be applied in tactile sensors, motion detection, physiological activity monitoring and mechanical energy scavenging. Pyroelectric wearable devices can be used to harvest energy from ambient temperature changes and detect physiological activity, such as respiration. Photovoltaic devices can scavenge energy from light to power wearable electronic devices and be

used as self-powered photo detectors.[129, 154, 182-195] There are also wearable devices based on multiple effects to scavenge energy from a range of stimuluses or work as multi-functional sensors.

Today, the energy shortage and environment pollution problems caused by the population explosion and growth in demand have become global challenges. There is also a need for self-powered systems in light of the Internet of Things and the vast number of connected devices and sensors. Nanogenerators are devices with simple structures which can scavenging energy from ambient environment and meet the demand. The mechanisms mentioned in this review confirm that the energy conversion performance of ferroelectric materials based nanogenerators can be regulated through tuning applied electric field due to the switchable polarisation in ferroelectric materials. The output performance of ferroelectric nanogenerators can be optimized by investigate the strength and switching property of the polarization. Furthermore, the polarization performance is closely connected with the domain structures of ferroelectrics and the domain structures are determined by the crystal structure, microstructure such as grain size and geometrical morphology of the ferroelectric materials. In addition, the energy scavenging performance can be improved by coupling multiple effects into a one-structured device that can be applied to harvesting mechanical, thermal and solar energy simultaneously and superimposed electrical output signals. Energy scavenging devices can be more smart, flexible, integrated, multifunctional and miniaturized which can be applied in smart wearable devices, multifunctional detectors and other self-powered devices, for example, oral electronic medicine, skin-interfaced sensors, internet of things, automatic drive and space detection. Finally, while ferroelectric materials-based

energy scavenging devices have been developed and a large research interest, the practical application and commercial potential is still need to be fully exploited.

Acknowledgments

This work was supported by the National Key R&D Project from Minister of Science and Technology in China (No. 2016YFA0202701), the National Natural Science Foundation of China (No. 52072041), External Cooperation Program of BIC, Chinese Academy of Sciences (No. 121411KYS820150028), the 2015 Annual Beijing Talents Fund (No. 2015000021223ZK32), Qingdao National Laboratory for Marine Science and Technology (No. 2017ASKJ01), and the University of Chinese Academy of Sciences (Grant No. Y8540XX2D2).

Received: ((will be filled in by the editorial staff))
Revised: ((will be filled in by the editorial staff))
Published online: ((will be filled in by the editorial staff))

[1] X. D. Wang, J. H. Song, J. Liu, Z. L. Wang, *Science* **2007**, *316*, 102.

[2] C. E. Chang, V. H. Tran, J. B. Wang, Y. K. Fuh, L. W. Lin, *Nano Lett.* **2010**, *10*, 726.

[3] X. S. Zhang, M. D. Han, R. X. Wang, F. Y. Zhu, Z. H. Li, W. Wang, H. X. Zhang, *Nano Lett.* **2013**, *13*, 1168.

[4] Valasek, J., *Phys. Rev.* **1921**, *17*, 475.

[5] J. F. Scott, *science* **2007**, *315*, 954.

[6] H. Takasu, *J. Electroceram.* **2000**, *4*, 327.

[7] M. N. Almadhoun, U. S. Bhansali, H. N. Alshareef, *J. Mater. Chem.* **2012**, *22*, 11196.

[8] K. T. Butler, J. M. Frost, A. Walsh, *Energy Environ. Sci.* **2015**, *8*, 838.

[9] R. C. Buchanan, J. Huang, *J. Eur. Ceram. Soc.* **1999**, *19*, 1467.

[10] W. D. Dong, P. Finkel, A. Amin, C. S. Lynch, *Appl. Phys. Lett.* **2012**, *100*, p.042903.1.

[11] Z. Y. Wang, K. Sun, P. T. Xie, Q. Hou, Y. Liu, Q. L. Gu, R. H. Fan, *Acta Mater.* **2020**, *185*, 412.

[12] Z. Y. Wang, H. Y. Li, H. Y. Hu, Y. Q. Fan, R. H. Fan, B. W. Li, J. X. Zhang, H. Liu, J. C. Fan, H. Hou, F. Dang, Z. K. Kou, Z. H. Guo, *Adv. Electron. Mater.* **2020**, *6*, 1.

[13] D. D. N. Setter, L. Eng, G. Fox, S. Gevorgian, *J. Appl. Phys* **2006**, *100*, 1.

[14] J. R. Gomah-Pettry, Amp Senda. Marchet Pascal, Mercurio Jean Pierre, *J. Eur. Ceram. Soc.* **2004**, *24*, 1165.

[15] H. Ting, K. Er-Jun, *Acta Phys. Sinica* **2018**, *67*, 1577011.

[16] P. Kim, N. M. Doss, J. P. Tillotson, P. J. Hotchkiss, M. J. Pan, S. R. Marder, J. Y. Li, J. P. Calame, J. W. Perry, *Acs Nano* **2009**, *3*, 2581.

[17] Y. Song, Y. Shen, H. Y. Liu, Y. H. Lin, M. Li, C. W. Nan, *J. Mater. Chem.***2012**, *22*, 8063.

[18] X. H. Dai, Z. Xu, D. Viehland, *Philos. Mag. B-Phys. Condensed Matter Statistical Mechanics Electronic Optical and Magnetic Properties* **1994**, *70*, 33.

[19] V. Bobnar, Z. Kutnjak, R. Pirc, A. Levstik, *Phys. Rev. B* **1999**, *60*, 6420.

[20] U. Chon, J. S. Shim, H. M. Jang, *J. Appl. Phys.* **2003**, *93*, 4769.

[21] K. Yu, Y. J. Niu, Y. C. Zhou, Y. Y. Bai, H. Wang, *J. Am. Ceram. Soc.* **2013**, *96*, 2519.

[22] C. A. Randall, D. J. Barber, R. W. Whatmore, *J. Mate. Sci.* **1987**, *22*, 925.

[23] V. Srinivasan, D. Sebastiani, *J. Phys. Chem. C* **2011**, *115*, 12631.

[24] C. S. Christopher J. Bartel, Bryan R. Goldsmith, Runhai Ouyang, Charles B. Musgrave, Luca M. Ghiringhelli, Matthias Scheffler, *Sci. Adv.* **2019**, *5*, 1.

[25] K. D. Budd, S. K. Dey, D. A. Payne, *Br. Ceram. Proceedings* **1985**, 107.

[26] K. I. Park, J. H. Son, G. T. Hwang, C. K. Jeong, J. Ryu, M. Koo, I. Choi, S. H. Lee, M. Byun, Z. L. Wang, K. J. Lee, *Adv. Mater.* **2014**, *26*, 2514.

[27] Y. Qi, J. Kim, T. D. Nguyen, B. Lisko, P. K. Purohit, M. C. McAlpine, *Nano Lett.* **2011**, *11*, 1331.

[28] D. Shen, J. H. Park, J. Ajitsaria, S. Y. Choe, H. C. Wikle, D. J. Kim, *J. Micromech. Microeng.* **2008**, *18*, 7.

[29] R. Theissmann, L. A. Schmitt, J. Kling, R. Schierholz, K. A. Schönau, H. Fuess, M. Knapp, H. Kungl, M. J. Hoffmann, *J. Appl. Phys.* **2007**, *102*, 0241111.

[30] A. Bogdanov, A. Mysovsky, C. Pickard, A. V. Kimmel, *Ferroelectrics (UK)* **2017**, *520*, 1.

[31] M. S. Chae, D. J. Shin, H. J. Kim, S. M. Koo, J. G. Ha, K. H. Cho, C. E. Seo, J. H. Koh, *Ferroelectrics (UK)* **2013**, *451*, 1.

[32]P. Sharma, S. Hajra, S. Sahoo, P. K. Rout, R. N. P. Choudhary, *J. Mater. Sci. Mater. Electron.* **2017**, *28*, 12048.

[33] J. F. Meng, R. S. Katiyar, G. T. Zou, X. H. Wang, *Phys. Status Solidi A-Appl. Res.* **1997**, *164*, 851.

[34] H. H. Kumar, C. M. Lonkar, K. Balasubramanian, *Appl. Phys. A-Mater. Sci. Process.* **2017**, *123*, 1.

[35] S. J. Zhang, R. Xia, T. R. Shrout, *J. Electroceram.* **2007**, *19*, 251.

[36] T. R. Shrout, S. J. Zhang, *J. Electroceram.* **2007**, *19*, 113.

[37] K. J. Choi, M. Biegalski, Y. L. Li, A. Sharan, J. Schubert, R. Uecker, P. Reiche, Y. B. Chen, X. Q. Pan, V. Gopalan, L. Q. Chen, D. G. Schlom, C. B. Eom, *Science* **2004**, *306*, 1005.

[38] S. Saha, T. P. Sinha, A. Mookerjee, *Phys. Rev. B* **2000**, *62*, 8828.

[39] J. Wang, J. B. Neaton, H. Zheng, V. Nagarajan, S. B. Ogale, B. Liu, D. Viehland, V. Vaithyanathan, D. G. Schlom, U. V. Waghmare, N. A. Spaldin, K. M. Rabe, M. Wuttig, R. Ramesh, *Science* **2003**, *299*, 1719.

[40] F. Kubel, H. Schmid, *Acta Crystallogr. Sect. B-Struct. Commun.* **1990**, *46*, 698.

[41] R. J. Zeches, M. D. Rossell, J. X. Zhang, A. J. Hatt, Q. He, C. H. Yang, A. Kumar, C. H. Wang, A. Melville, C. Adamo, G. Sheng, Y. H. Chu, J. F. Ihlefeld, R. Erni, C. Ederer, V. Gopalan, L. Q. Chen, D. G. Schlom, N. A. Spaldin, L. W. Martin, R. Ramesh, *Science* **2009**, *326*, 977.

[42] E. Hollenstein, D. Damjanovic, N. Setter, *J. Eur. Ceram. Soc.* **2007**, *27*, 4093.

[43] Z. M. Dang, Y. H. Lin, C. W. Nan, *Adv. Mater.***2003**, *15*, 1625.

[44] M. Y. Li, H. J. Wondergem, M. J. Spijkman, K. Asadi, I. Katsouras, P. W. M. Blom, D. M. de Leeuw, *Nat. Mater.* **2013**, *12*, 433.

[45] V. Vivekananthan, N. R. Alluri, Y. Purusothaman, A. Chandrasekhar, S. J. Kim, *Nanoscale* **2017**, *9*, 15122.

[46] G. Vats, A. Kumar, N. Ortega, C. R. Bowen, R. S. Katiyar, *Energy & Environmental Science* **2016**, *9*, 1335.

[47] R. Ghane-Motlagh, P. Woias, *Smart Mater. Struct.* **2019**, *28*, 1.

[48] P. G. Kang, B. K. Yun, K. D. Sung, T. K. Lee, M. Lee, N. Lee, S. H. Oh, W. Jo, H. J. Seog, C. W. Ahn, I. W. Kim, J. H. Jung, *RSC Adv.* **2014**, *4*, 29799.

[49] A. Koka, Z. Zhou, H. A. Sodano, *Energy Environ. Sci.* **2014**, *7*, 288.

[50] G. Zhang, P. Zhao, X. Zhang, K. Han, T. Zhao, Y. Zhang, C. K. Jeong, S. Jiang, S. Zhang, Q. Wang, *Energy Environ. Sci.* **2018**, *11*, 2046.

[51] R. Zhao, N. Ma, K. Song, Y. Yang, *Adv. Funct. Mater.* **2019**, *30*, 1.

[52] J. T. C. R. Bowen, E. LeBoulbar, D. Zabek, A. Chauhanc and R. Vaishc, *Energy Environ. Sci.* **2014**, *7*, 3836.

[53] D. Damjanovic, *Rep. Prog. Phys.* **1998**, *61*, 1267.

[54] C. W. Jie Wang, Yejing Dai, Zhihao Zhao, Aurelia Wang, Tie jun Zhang, Zhong Lin Wang, *Nat. Commun.* **2007**, *8*, 1.

[55] J. B. Yu, X. J. Hou, M. Cui, N. Zhang, S. N. Zhang, J. He, X. J. Chou, *Mater. Lett.***2020**, *269*, 5.

[56] C. R. Bowen, H. A. Kim, P. M. Weaver, S. Dunn, *Energy Environ. Sci.* **2014**, *7*, 25.

[57] N. S. Shenck, J. A. Paradiso, *IEEE Micro* **2001**, *21*, 30.

[58] G. R. Chen, Y. Z. Li, M. Bick, J. Chen, *Chem. Rev.* **2020**, *120*, 3668.

[59] W. Cao, F. Nie, W. Huang, Q. Gu, W. Yu, *Electron. Components Mater.* **2016**, *35*, 6.

[60] A. Hadni, *Journal of Physics E-Scientific Instruments* **1981**, *14*, 1233.

[61] Y. Yuan, Z. Xiao, B. Yang, J. Huang, *J. Mater. Chem. A* **2014**, *2*, 6027.

[62] S. Y. Yang, J. Seidel, S. J. Byrnes, P. Shafer, C. H. Yang, M. D. Rossell, P. Yu, Y. H. Chu, J. F. Scott, J. W. Ager, 3rd, L. W. Martin, R. Ramesh, *Nat Nanotech.* **2010**, *5*, 143.

[63] R. M. W T.H Koch, W Ruppel and P Wurfel, *Sohd State Commumcatrons,* **1975**, *17*, 847.

[64] Frost, Jarvist, M., Walsh, Aron, Butler, Keith, T., *Energy Environ. Sci.* **2015**, *8*, 838.

[65] H. Huang, *Nat. Photon.* **2010**, *4*, 134.

[66] M. Nakamura, S. Horiuchi, F. Kagawa, N. Ogawa, T. Kurumaji, Y. Tokura, M. Kawasaki, *Nat. Commun.* **2017**, *8*, 281.

[67] Y. Ji, K. Zhang, Z. L. Wang, Y. Yang, *Energy Environ. Sci.* **2019**, *12*, 1231.

[68] K. Uchino, *Ferroelectric Devices*, CRC Press, Inc., **2000**.

[69] A. E. Feuersanger, A. K. Hagenlocher, A. L. Solomon, *J. Electrochem. Soc.* **1964**, *111*, 1387.

[70] P. M. Heyman, G. H. Heilmeier, *P. IEEE.* **1966**, *54*, 842.

[71] R. Zuleeg, H. H. Wieder, *Solid-State Electron.* **1966**, *9*, 657.

[72] O. Tada, Y. Shintani, Y. Yoshida, *J. Appl. Phys.* **1969**, *40*, 498.

[73] J. C. Crawford, *Ferroelectrics (UK)* **1970**, *1*, 23.

[74] E. V. Bursian, Y. G. Girshberg, K. V. Makarov, O. I. Zaikovskii, *Fiz. Tverd. Tela (USSR)* **1970**, *12*, 1850.

[75] M. H. Francombe, *Thin Solid Films* **1972**, *13*, 413.

[76] A. W. Stephens, T. J. Zrebiec, V. S. Ban, *Mater. Res. Bull.* **1974**, *9*, 1427.

[77] J. F. Scott, C. A. Paz de Araujo, *Science* **1989**, *246*, 1400.

[78] R. J. N. G. J. M. J E Tibballs, *J. Phys. C: Solid State Phys* **1982**, *15*, 37.

[79] J. C. Slater, *Ferroelectrics (UK)* **1987**, *71*, 25.

[80] B. Luo, X. Wang, E. Tian, H. Gong, Q. Zhao, Z. Shen, Y. Xu, X. Xiao, L. Li, *ACS Appl. Mater. Inter.* **2016**, *8*, 3340.

[81] L. Xu, Y. D. Hu, C. He, Z. J. Wang, X. M. Yang, X. F. Long, J. J. Fu, *Crystal Growth Design* **2019**, *19*, 4902−4907.

[82] N. Dix, R. Muralidharan, J. M. Rebled, S. Estradé, F. Sánchez, *Acs Nano* **2010**, *4*, 4955.

[83] C. E. J. B. Neaton, U. V. Waghmare, N. A. Spaldin, and K. M. Rabe, *Phys. Rev. b* **2005**, *71*, 1.

[84] A. Pramanick, S. O. Diallo, O. Delaire, S. Calder, A. D. Christianson, X. L. Wang, J. A. Fernandez-Baca, *Phys. Rev. B* **2013**, *88*, 1.

[85] P. J. L. L. A. Bursill, *Nat. Commun.* **1984**, *311*, 550.

[86] V. V. Osipov, D. A. Kiselev, E. Y. Kaptelov, S. V. Senkevich, I. P. Pronin, *Phys. Solid State* **2015**, *57*, 1793.

[87] H. Lu, C. W. Bark, D. Esque de los Ojos, J. Alcala, C. B. Eom, G. Catalan, A. Gruverman, *Science* **2012**, *336*, 59.

[88] D. Bolten, U. Bottger, T. Schneller, M. Grossmann, O. Lohse, R. Waser, *Appl. Phys. Lett.s* **2000**, *77*, 3830.

[89] O. Boser, *J. Appl. Phys.* **1987**, *62*, 1344.

[90] K. Kushida‐Abdelghafar, H. Miki, K. Torii, Y. Fujisaki, *Appl. Phys. Lett.* **1996**, *69*, 3188.

[91] Q. M. Zhang, H. Wang, N. Kim, L. E. Cross, *J. Appl. Phys.* **1994**, *75*, 454.

[92] F. Xu, S. Trolier-McKinstry, W. Ren, B. Xu, Z. L. Xie, K. J. Hemker, *J. Appl. Phys.* **2001**, *89*, 1336.

[93] P. M. Chaplya, G. P. Carman, *Journal of Applied Physics* **2001**, *90*, 5278.

[94] J. Karthik, L. W. Martin, *Phys. Rev. B* **2011**, *84*, 024102.

[95]Y. Bai, T. Siponkoski, J. Peräntie, H. Jantunen, J. Juuti, *Appl. Phys. Lett.* **2017**, *110*, 063903.

[96] H. Matsuo, Y. Kitanaka, R. Inoue, Y. Noguchi, M. Miyayama, T. Kiguchi, T. J. Konno, *Phys. Rev. B* **2016**, *94*.

[97] Y. Bai, G. Vats, J. Seidel, H. Jantunen, J. Juuti, *Adv. Mater.* **2018**, *30*, e1803821.

[98] M. Davis, D. Damjanovic, N. Setter, *Phys. Rev. B* **2006**, *73*, 1.

[99] V. Dvořák, Y. Ishibashi, *Tokyo Sugaku Kaisya Zasshi* **1976**, *41*, 1621.

[100] N. N. Kristoffel, P. I. Konsin, *Ferroelectrics (UK)* **1973**, *6*, 3.

[101] O. Tikhomirov, H. Jiang, J. Levy, *Appl. Phys. Lett.* **2000**, *77*, 2048.

[102] L. Wu, X. Wang, H. Gong, Y. Hao, Z. Shen, L. Li, *J. Mater. Chem. C* **2015**, *3*, 750.

[103] C. J. Chen, W. Zhu, J. H. Chao, A. Shang, Y. G. Lee, R. Liu, S. Yin, M. Dubinskii, R. C. Hoffman, *J. Alloys Compd.* **2019**, *804*, 35.

[104] G. Zhang, M. Li, H. Li, Q. Wang, S. Jiang, *Energy Tech.* **2018**, *6*, 791.

[105] X. Hu, K. Yi, J. Liu, B. Chu, *Energy Tech.* **2018**, *6*, 849.

[106] H. Zhu, S. Pruvost, P. J. Cottinet, D. Guyomar, *Appl. Phys. Lett.* **2011**, *98*.

[107] C. R. Bowen, V. Y. Topolov, A. N. Isaeva, P. Bisegna, *CrystEngComm* **2016**, *18*, 5986.

[108] S. E. Park, T. R. Shrout, *J. Appl. Phys.* **1997**, *82*, 1804.

[109] Z. Kutnjak, J. Petzelt, R. Blinc, *Nature* **2006**, *441*, 956.

[110] Z. Xie, B. Peng, J. Zhang, X. Zhang, Z. Yue, L. Li, S. E. Trolier-McKinstry, *J. Am. Ceram. Soc.* **2015**, *98*, 2968.

[111] X. Gao, J. Wu, Y. Yu, Z. Chu, H. Shi, S. Dong, *Adv. Funct. Mater.s* **2018**, *28*, 1706895.

[112] F. Y. Lee, H. R. Jo, C. S. Lynch, L. Pilon, *Smart Mater.s Struct.* **2013**, *22*, 025038

[113] K. U. Hinchet Ronan, Falconi Christian, Kim Sang-Woo, *Mater. Today* **2019**, *21*, 611.

[114] T. Zheng, J. G. Wu, D. Q. Xiao, J. G. Zhu, *Prog. Mater. Sci.* **2018**, *98*, 552.

[115] Y. Zhang, X. F. Liu, G. Wang, Y. Li, S. J. Zhang, D. W. Wang, H. J. Sun, *J. Alloy. Compd.* **2020**, *825*, 1.

[116] R. W. C. Lewis, C. R. Bowen, V. Y. Topolov, D. W. E. Allsopp, Integr. Ferroelectr. 2012, 133, 103.

[117] D. B. Deutz, J. A. Pascoe, B. Schelen, S. van der Zwaag, D. M. de Leeuw, P. Groen, *Mater. Horizons* **2018**, *5*, 444.

[118] J. I. Roscow, H. Pearce, H. Khanbareh, S. Kar-Narayan, C. R. Bowen, *Eur Phys J-Spec Top* **2019**, *228*, 1537.

[119] S. G. K. R. Xu, presented at *PowerMEMS*, Atlanta, GA, USA, December 2-5, 2012, 2012.

[120] Y. H. Jing Yan, Xiaole Yu, Mupeng Zheng, Mankang Zhu, *J. Eur. Ceram. Soc.* **2019**, *39*, 2666.

[121] S. Priya, *IEEE Transactions on Ultrasonics, Ferroelectrics, and Frequency Control* **2010**, *57*, 2610.

[122] M. J. A. Cecilia D Richards, David F Bahr and Robert F Richards, *J. Micromechan. Microeng.* **2004**, *14*, 717.

[123] I. T. Seo, C. H. Choi, D. Song, M. S. Jang, B. Y. Kim, S. Nahm, Y. S. Kim, T. H. Sung, H. C. Song, S. Zhang, *J. Am. Ceram. Soc.* **2013**, *96*, 1024.

[124] X. Y. Zhao, H. Cao, Y. P. Guo, H. S. Luo, *Mater. Sci. Eng. B* **2002**, *96*, 254.

[125] K. Xu, J. Li, X. Lv, J. Wu, X. Zhang, D. Xiao, J. Zhu, *Adv. Mater.* **2016**, *28*, 8519.

[126] P. Li, J. Zhai, B. Shen, S. Zhang, X. Li, F. Zhu, X. Zhang, *Adv. Mater.* **2018**, *30*.

[127] K. I. Park, J. H. Son, G. T. Hwang, C. K. Jeong, J. Ryu, M. Koo, I. Choi, S. H. Lee, M. Byun, Z. L. Wang, K. J. Lee, *Adv. Mater.* **2014**, *26*, 2514.

[128] J. Kwon, W. Seung, B. K. Sharma, S.-W. Kim, J.-H. Ahn, *Energy Environ. Sci.* **2012**, *5*, 8970.

[129] X. Chen, X. Li, J. Shao, N. An, H. Tian, C. Wang, T. Han, L. Wang, B. Lu, *Small* **2017**, *13*.

[130] J. H. Lee, K. Y. Lee, B. Kumar, N. T. Tien, N. E. Lee, S. W. Kim, *Energy Environ. Sci.* **2013**, *6*, 169.

[131] J. Yan, Y. G. Jeong, *ACS Appl. Mater. Inter.* **2016**, *8*, 15700.

[132] J. Lee, S. W. Kim, S. H. Jeong, Y. M. Choi, S. Y. Lee, *Energy Environ. Sci.* **2018**, *11*, 1425.

[133] A. R. Monali Mishra, Sukalyan Dash, Somdutta Mukherjee, *7th National Conference on Processing and Characterization of Materials (NCPCM 2017)*, Rourkela, INDIA, 2018. [134] K. Park, S. Xu, Y. Liu, G.-T. Hwang, S.-J. L. Kang, Z. L. Wang, K. J. Lee, *Nano Lett.* **2010**, *10*, 4939.

[135] X. L. Chen, Y. C. Ding, H. M. Tian, X. M. Li, Y. P. Zhou, *IEEE NANO 2015 15th International Conference on Nanotechnology*, Rome, Italy, JUL 27-30, 2015, 2015.

[136] Lang, B. Sidney, *Phys. Today* **2005**, *58*, 31.

[137] R. W. Whatmore, *Rep. Prog. Phys.* **1986**, *49*, 1335.

[138] S. Pandya, J. Wilbur, J. Kim, R. Gao, A. Dasgupta, C. Dames, L. W. Martin, *Nat. Mater.* **2018**, *17*, 432.

[139] J. T. C.R. Bowen, E. Le Boulbar, D. Zabek, V.Yu. Topolov *Mater. Lett.* **2015**, *138*, 243.

[140] Y. Zhang, M. Xie, J. Roscow, Y. Bao, K. Zhou, D. Zhang, C. R. Bowen, *J. Mater. Chem. A.* **2017**, *5*, 6569.

[141] K. W. Zhang, Z. L. Wang, Y. Yang, *Nano Energy*, **2019**, *55*, 534.

[142] Y. Zhang, M. Xie, J. Roscow, Y. Bao, K. Zhou, D. Zhang, C. R. Bowen, *J. Mater. Chem. A.* **2017**, *5*, 6569.

[143] S. Pandya, G. Velarde, L. Zhang, J. D. Wilbur, A. Smith, B. Hanrahan, C. Dames, L. W. Martin, *NPG Asia Materials* **2019**, *11*, 1.

[144] S. Mohammadi, A. Khodayari, *Smart Mater. Res.* **2012**, *2012*, 1.

[145] R. B. Olsen, J. M. Briscoe, D. A. Bruno, W. F. Butler, *Ferroelectrics* **1981**, *38*, 975

[146] G. Sebald, S. Pruvost, D. Guyomar, *Smart Mate. Struct.* **2008**, *17*, 1

[147] R. B. Olsen, D. A. Bruno, J. M. Briscoe, *J. Appl. Phys.* **1985**, *58*, 4709.

[148] B. Bhatia, A. R. Damodaran, H. Cho, L. W. Martin, W. P. King, *J. Appl. Phys.* **2014**, *116*, 1945091.

[149] I. M. McKinley, L. Pilon, *Appl. Phys. Lett.* **2013**, *102*, 0239061.

[150] R. V. Gaurav Vats, and Chris R. Bowen, *J. Appl. Phys.* **2014**, *115*, 1.

[151] B. M. Hanrahan, F. Sze, A. N. Smith, N. R. Jankowski, *International Journal of Energy Research* **2017**, *41*, 1880.

[152]A. M. Stark, 2020, https://www.llnl.gov/news/technique-harvests-waste-heat-untapped-sources .

[153] S. N. Alexandra Garraud, Alain Giani, Philippe Combette, in *2014 Symposium on Design, Test, Integration and Packaging of MEMS/MOEMS (DTIP)*, IEEE, Piscataway, NJ, USA, Cannes, France 2014, 356.

[154] H. Xue, Q. Yang, D. Wang, W. Luo, W. Wang, M. Lin, D. Liang, Q. Luo, *Nano Energy* **2017**, *38*, 147.

[155] J. Yang, X. Hao, *J. Am. Ceram. Soc.* **2019**, *102*, 6817.

[156] H. Zhang, S. Zhang, G. Yao, Z. Huang, Y. Xie, Y. Su, W. Yang, C. Zheng, Y. Lin, *ACS Appl. Mater. Inter.* **2015**, *7*, 28142.

[157] J. H. Jia, S. B. Guo, S. G. Yan, F. Cao, C. H. Yao, X. L. Dong, G. S. Wang, *Appl. Phys. Lett.*, **2019**, *114*, 03292.

[158] A. R. Damodaran, S. Pandya, Y. B. Qi, S. L. Hsu, S. Liu, C. Nelson, A. Dasgupta, P. Ercius, C. Ophus, L. R. Dedon, J. C. Agar, H. L. Lu, J. L. Zhang, A. M. Minor, A. M. Rappe, L. W. Martin, *Nat. Commun.* **2017**, *8*, 8.

[159] A. Ianculescu, I. Pintilie, C. A. Vasilescu, M. Botea, A. Iuga, A. Melinescu, N. Dragan, L. Pintilie, *Ceram. Inter.* **2016**, *42*, 10338.

[160] K. S. Srikanth, V. P. Singh, R. Vaish, *International J. Appl. Ceram. Tech.* **2018**, *15*, 140.

[161] J. Zhang, X. Su, M. Shen, Z. Dai, L. Zhang, X. He, W. Cheng, M. Cao, G. Zou, *Sci. Rep.* **2013**, *3*, 6.

[162] I. Grinberg, D. V. West, M. Torres, G. Gou, D. M. Stein, L. Wu, G. Chen, E. M. Gallo, A. R. Akbashev, P. K. Davies, J. E. Spanier, A. M. Rappe, *Nature* **2013**, *503*, 509.

[163] W. Ji, K. Yao, Y. C. Liang, *Adv. Mater.* **2010**, *22*, 1763.

[164] J. E. Spanier, V. M. Fridkin, A. M. Rappe, A. R. Akbashev, A. Polemi, Y. Qi, Z. Gu, S. M. Young, C. J. Hawley, D. Imbrenda, G. Xiao, A. L. Bennett-Jackson, C. L. Johnson, *Nat. Photon.* **2016**, *10*, 611.

[165] S. L. T. Choi, Y. J. Choi, V. Kiryukhin, S. W. Cheong, *Science* **2009**, *324*, 63.

[166] H. T. Yi, T. Choi, S. G. Choi, Y. S. Oh, S. W. Cheong, *Adv. Mater.* **2011**, *23*, 3403.

[167] H. Matsuo, Y. Noguchi, M. Miyayama, *Nat. Commun.* **2017**, *8*, 2071.

[168] J. A. G. E. Monroy, E. Muñoz, I. Izpura, F. J. Sánchez, M. A. Sánchez-García, E. Calleja Dpt. Ingeniería Electrónica, E.T.S.I. Telecomunicación, Politécnica, Ciudad Universitaria, B. Beaumont, Pierre Gibart, *Inter. J. Nitride Semiconductor Res.* **1997**, *2*, 1.

[169] X. Liu, L. L. Gu, Q. P. Zhang, J. Y. Wu, Y. Z. Long, Z. Y. Fan, *Nat. Commun.* **2014**, *5*, 9.

[170] L. Hu, Y. Jian, M. Liao, H. Xiang, X. Gong, L. Zhang, X. Fang, *Adv. Mater.* **2012**, *24*, 2305.

[171] L. X. Zheng, K. Hu, F. Teng, X. S. Fang, *Small* **2017**, *13*, 10.

[172] Y. Bai, G. Vats, J. Seidel, H. Jantunen, J. Juuti, *Adv. Mater.* **2018**, *30*, 1.

[173] N. Ma, Y. Yang, *Nano Energy* **2019**, *60*, 95.

[174] J. Qi, N. Ma, X. Ma, R. Adelung, Y. Yang, *ACS Appl. Mater. Inter.* **2018**, *10*, 13712. [175] M. Shoaib, X. Zhang, X. Wang, H. Zhou, T. Xu, X. Wang, X. Hu, H. Liu, X. Fan, W. Zheng, T. Yang, S. Yang, Q. Zhang, X. Zhu, L. Sun, A. Pan, *J. Am. Chem. Soc.* **2017**, *139*, 15592.

[176] A. Quattropani, A. S. Makhort, M. V. Rastei, G. Versini, G. Schmerber, S. Barre, A. Dinia, A. Slaoui, J. L. Rehspringer, T. Fix, S. Colis, B. Kundys, *Nanoscale* **2018**, *10*, 13761.

[177] C. X. Zhang, T. Shen, D. Guo, L. M. Tang, K. Yang, H. X. Deng, *InfoMat* **2020**, *2*, 1034.

[178] S. S Wang, L. N. Li, C. M Ji, Z. H. Sun, Z. Y. Wu, M. C. Hong, and J. H. Luo, *J. Am. Chem. Soc.* **2019**, *141*, 7693.

[179] S. H. Wang , Z. L. Wang and Ya Yang, *Adv. Mater.* **2016**, *28*, 2881.

[180] K. Song, R. Zhao, Z. L. Wang, Y. Yang, *Adv. Mater.* **2019**, *31*, e1902831.

[181] K. Zhang, S. Wang, Y. Yang, *Adv. Energy Mater.* **2016**, *7*, 8.

[182] M. K. Jonghwa Park, Youngoh Lee, Heon Sang Lee, Hyunhyub Ko, *Sci. Adv.* **2015**, *1*, 1.

[183] K. Zhao, B. Ouyang, C. R. Bowen, Z. L. Wang, Y. Yang, *Nano Energy* **2020**, *71*, 104632.

[184] Y. Zhang, M. Wu, Q. Zhu, F. Wang, H. Su, H. Li, C. Diao, H. Zheng, Y. Wu, Z. L. Wang, *Adv. Funct. Mater.* **2019**, *29*, 1904259.

[185] Y. Chen, Y. Zhang, F. Yuan, F. Ding, O. G. Schmidt, *Adv. Electron. Mater.* **2017**, *3*, 1600540.

[186] H. Li, C. S. L. Koh, Y. H. Lee, Y. Zhang, G. C. Phan-Quang, C. Zhu, Z. Liu, Z. Chen, H. Y. F. Sim, C. L. Lay, Q. An, X. Y. Ling, *Nano Energy* **2020**, *73*, 104723.

[187] X. Hu, F. Li, Y. Song, *ACS Energy Lett.* **2019**, *4*, 1065.

[188] F. Cao, W. Tian, M. Wang, H. Cao, L. Li, *Adv. Funct. Mater.* **2019**, *29*, 1901280.

[189] P. Yu, W. Liu, C. Gu, X. Cheng, X. Fu, *Sensors (Basel)* **2016**, *16*.

[190] B. Dudem, D. H. Kim, L. K. Bharat, J. S. Yu, *Appl. Energy* **2018**, *230*, 865.

[191] M. H. You, X. X. Wang, X. Yan, J. Zhang, W.-Z. Song, M. Yu, Z.-Y. Fan, S. Ramakrishna, Y. Z. Long, *J.Mater. Chem. A* **2018**, *6*, 3500.

[192] N. Ma, K. Zhang, Y. Yang, *Adv. Mater.* **2017**, *29*, 1703694.

[193] W. Wu, X. Wang, X. Han, Z. Yang, G. Gao, Y. Zhang, J. Hu, Y. Tan, A. Pan, C. Pan, *Adv. Mater.* **2019**, *31*, e1805913.

[194] Y. J. Ko, D. Y. Kim, S. S. Won, C. W. Ahn, I. W. Kim, A. I. Kingon, S. H. Kim, J. H. Ko, J. H. Jung, *ACS Appl. Mater. Inter.* **2016**, *8*, 6504.

[195] D. B. Deutz, N. T. Mascarenhas, J. B. J. Schelen, D. M. de Leeuw, S. van der Zwaag, P. Groen, *Ad. Funct. Mater.* **2017**, *27*, 1700728.

[196] L. Xu, B. Su, Y. Hu, C. He, Z. Wang, X. Yang, X. Long, J. Fu, *Crystal Growth & Design* **2019**, *19*, 4902.

[197] J. F. Li, K. Wang, F. Y. Zhu, L. Q. Cheng, F. Z. Yao, D. J. Green, *J. Am. Ceram. Soc.* **2013**, *96*, 3677.

[198] K. Zhang, Y. Wang, Z. L. Wang, Y. Yang, *Nano Energy* **2019**, *55*, 534.

[199] R. Zhao, N. Ma, K. Song, Y. Yang, *Adv. Funct. Mater.* **2019**, *30*, 1906232.

[200] A. Quattropani, A. S. Makhort, M. V. Rastei, G. Versini, G. Schmerber, S. Barre, A. Dinia, A. Slaoui, J. L. Rehspringer, T. Fix, S. Colis, B. Kundys, *Nanoscale* **2018**, *10*, 13761.

FIGURE CAPTIONS

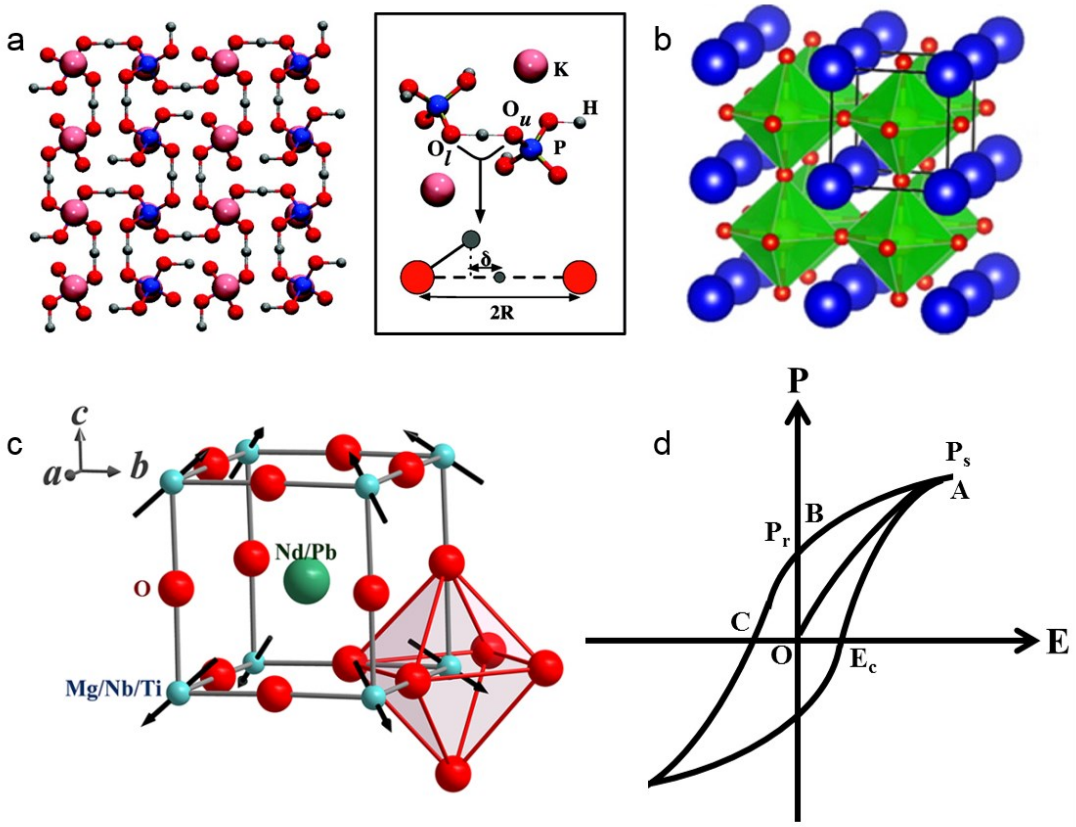

Figure 1. Ferroelectric structures and spontaneous polarization. a) Schematic of KDP structure. Reproduced with permission.[23] Copyright 2011, American Chemical Society. Perovskite structure. Reproduced with permission.[80] Copyright 2016, America Chemical Society. c) Schematic of spontaneous polarization of perovskite Structure. Reproduced with permission.[196] Copyright 2019, American Chemical Society. d) Polarisation-Electric field (P-E) hysteresis loop of a ferroelectric material.

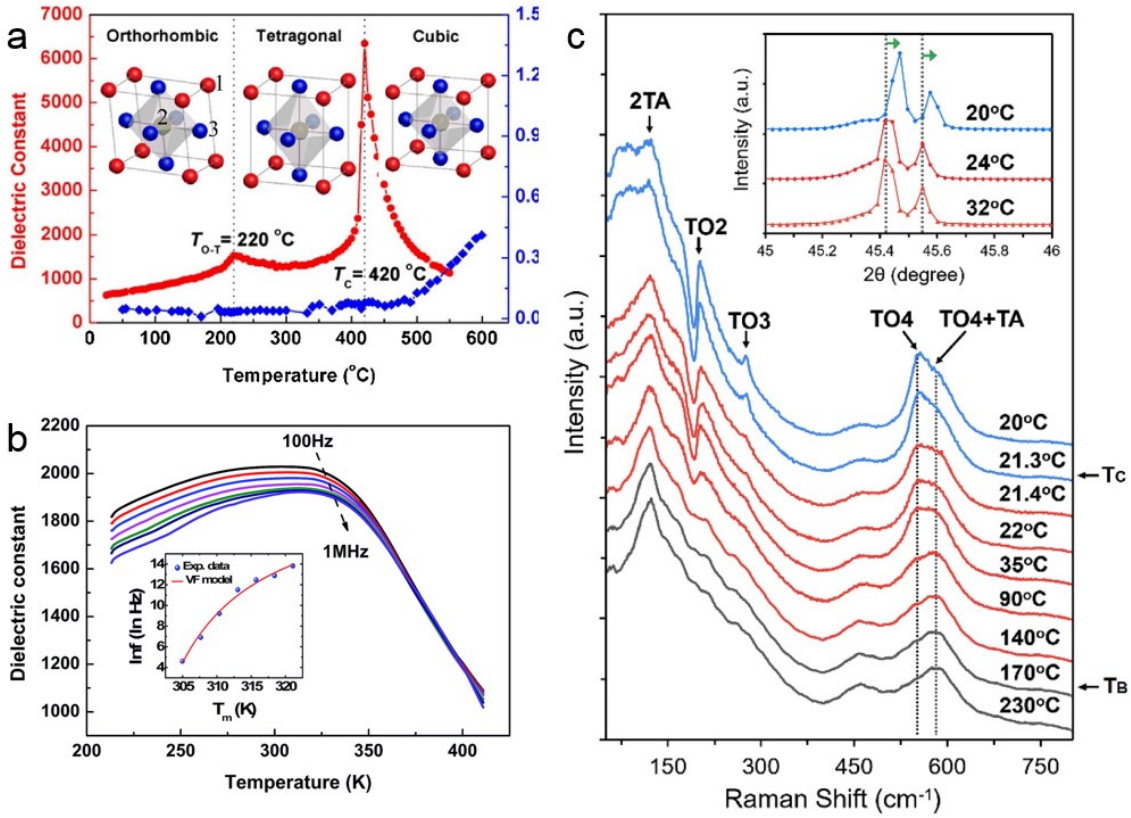

Figure 2. a) Normal ferroelectric phase transition. Temperature-dependent dielectric permittivity and loss of $K_{0.5}Na_{0.5}NbO_3$ ceramics. Relxor ferroelectric phase transition. Reproduced with permission.[197] Copyright 2013, American Chemical Society. b) Temperature and frequency dependent dielectric constant of the $0.6BaTiO_3@0.4SrTiO_3$ bulk ceramic. Reproduced with permission.[102] Copyright 2015, The Royal Society of Chemistry. c) The Raman spectra of $KTa_{0.61}Nb_{0.39}O_3$ at different temperatures. Reproduced with permission.[103] Copyright 2019, Elsevier.

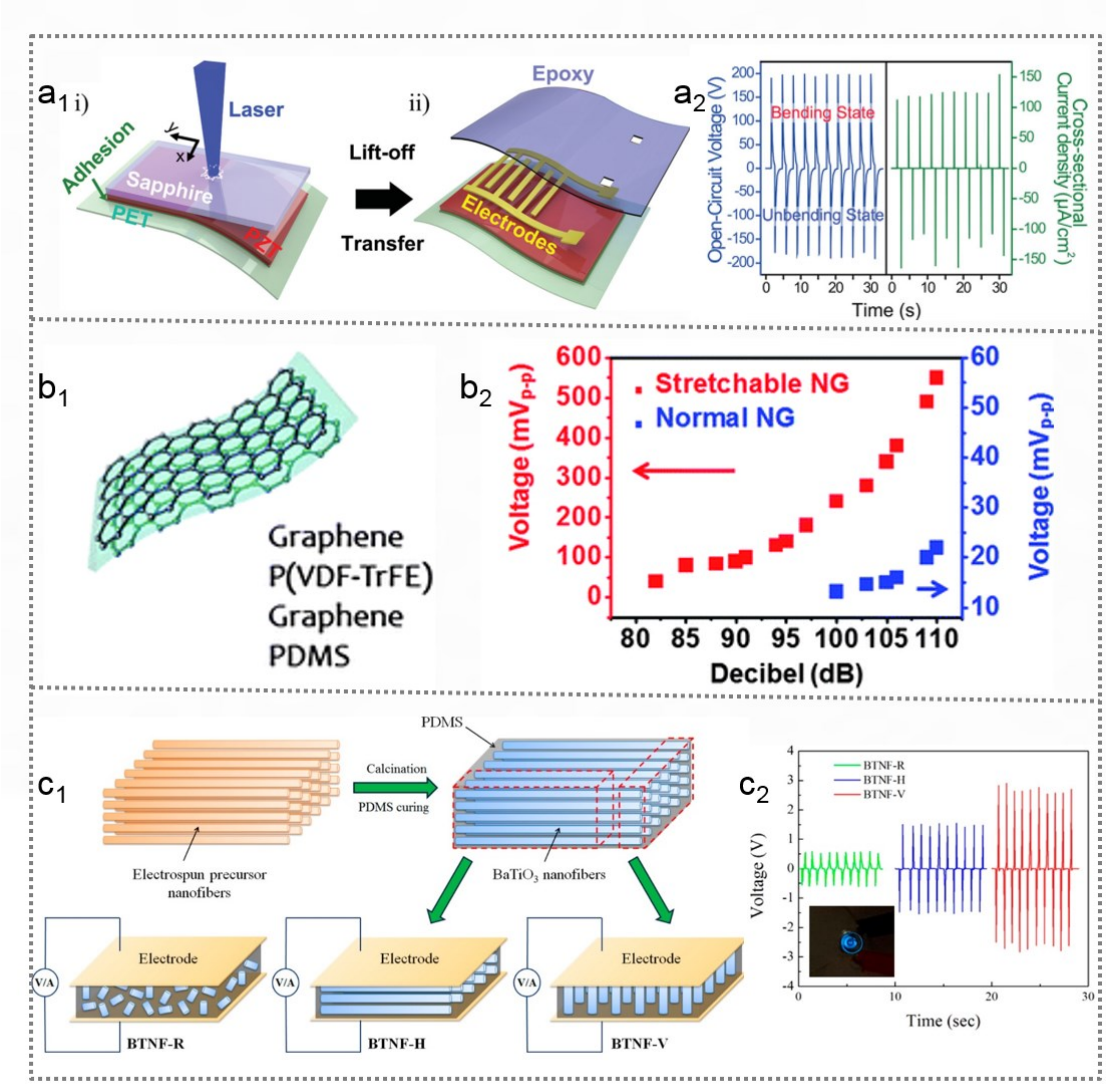

Figure 3. Piezoelectric nanogenerators. a) PZT based piezoelectric nanogenerator. a_1) Schematic of the preparing process for the flexible and large-area PZT thin film-based NG using the LLO method, a_2) The open-circuit voltage and cross-sectional current density measured from PZT thin film nanogenerator. Reproduced with permission.[127] Copyright 2014, Wiley-VCH. b) P(VDF-TrFE) based flexible nanogenerator, b_1) illustration of the stretchable nanogenerator based on P(VDF-TrFE), b_2) comparison of the piezoelectric peak-to-peak output voltage between the stretchable and the normal nanogenerators under the same sound wave pressure. Reproduced with permission.[130] Copyright 2013, Royal Society of Chemistry. c) $BaTiO_3$ nanofiber nanogenerator, c_1) Schematic of fabrication procedure of $BaTiO_3$-based nanogenerators, c_2) Output voltage of $BaTiO_3$/PDMS nanogenerator. Reproduced with permission.[131] Copyright 2016, America Chemical Society.

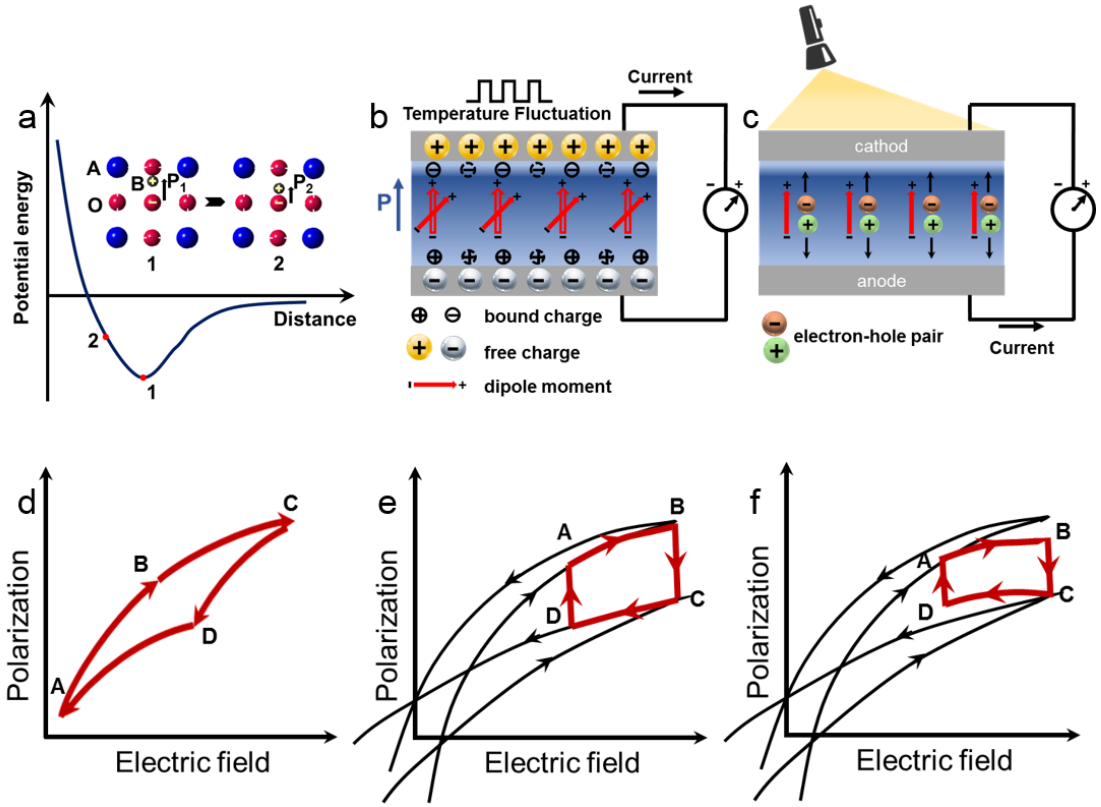

Figure 4. Schematic of pyroelectric effect and ferroelectric photovoltaic effect. a) Schematic of physical source of pyroelectric effect.[137] b) Schematic of charge generation behaviour of pyroelectric effect. c) Schematic of ferroelectric photovoltaic effect. The schematic diagrams of (d) pyroelectric Carnot Cycle, (e) pyroelectric Olsen Cycle, (f) pyroelectric Brayton Cycle.

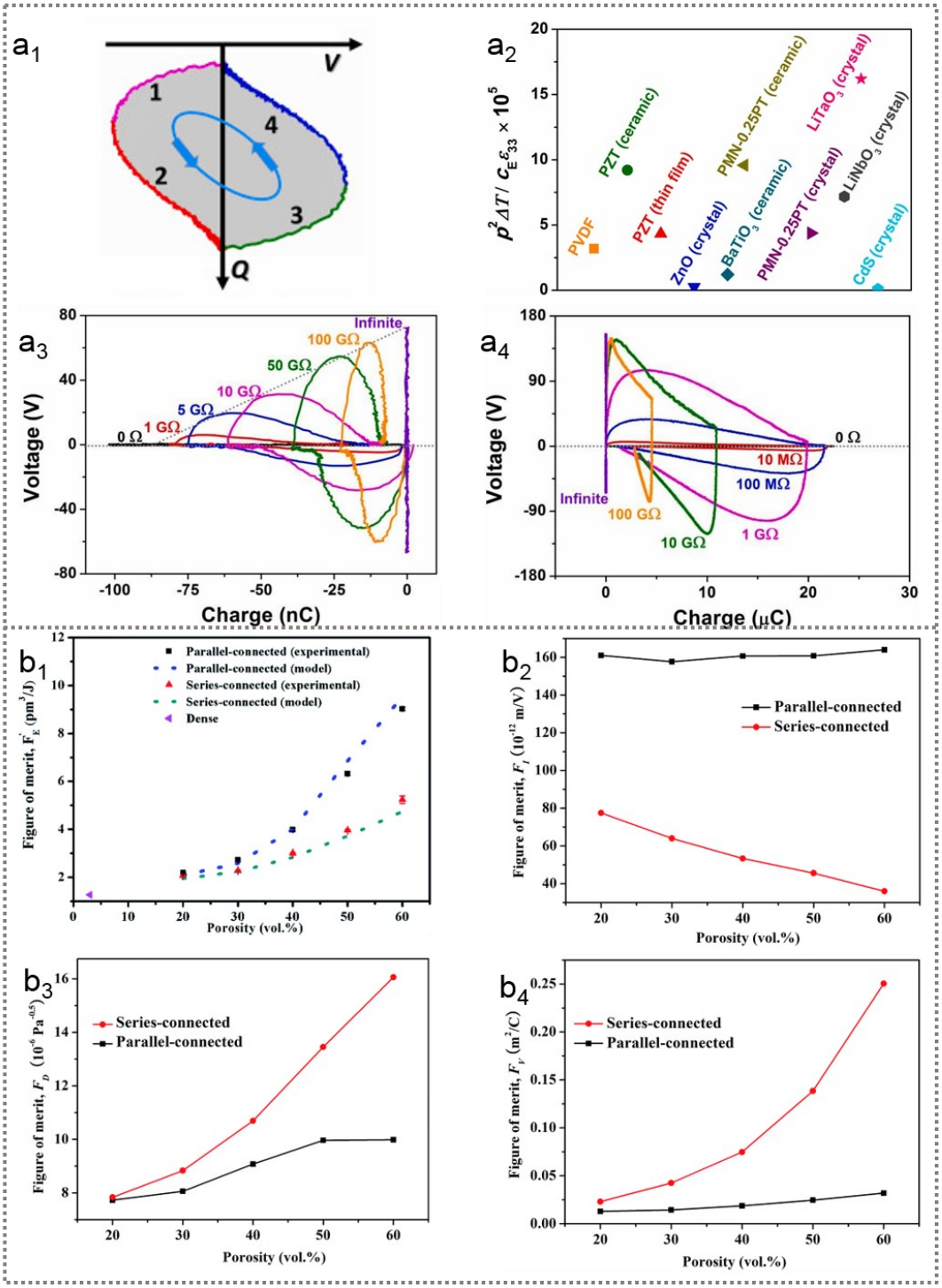

Figure 5. Figures of merits for pyroelectric nanogenerators. a) a$_1$) Charge-voltage (Q-V) cycle of a pyroelectric nanogenerator, a$_2$) Figure-of merit (FE") for different types of pyroelectric materials, a$_3$, a$_4$) Q-V cycles of a$_3$) PVDF device and a$_4$) PZT device under different load resistances. Reproduced with permission.[198] Copyright 2019, Elsevier. b) b$_1$) Porosity dependence of experimental and modelling pyroelectric figure of merit of porous PZT ceramics, b$_2$) Current responsivity F_I, b$_3$) F_D, b$_4$) voltage responsivity F_V. Reproduced with permission.[142] Copyright 2017, Royal Society of Chemistry.

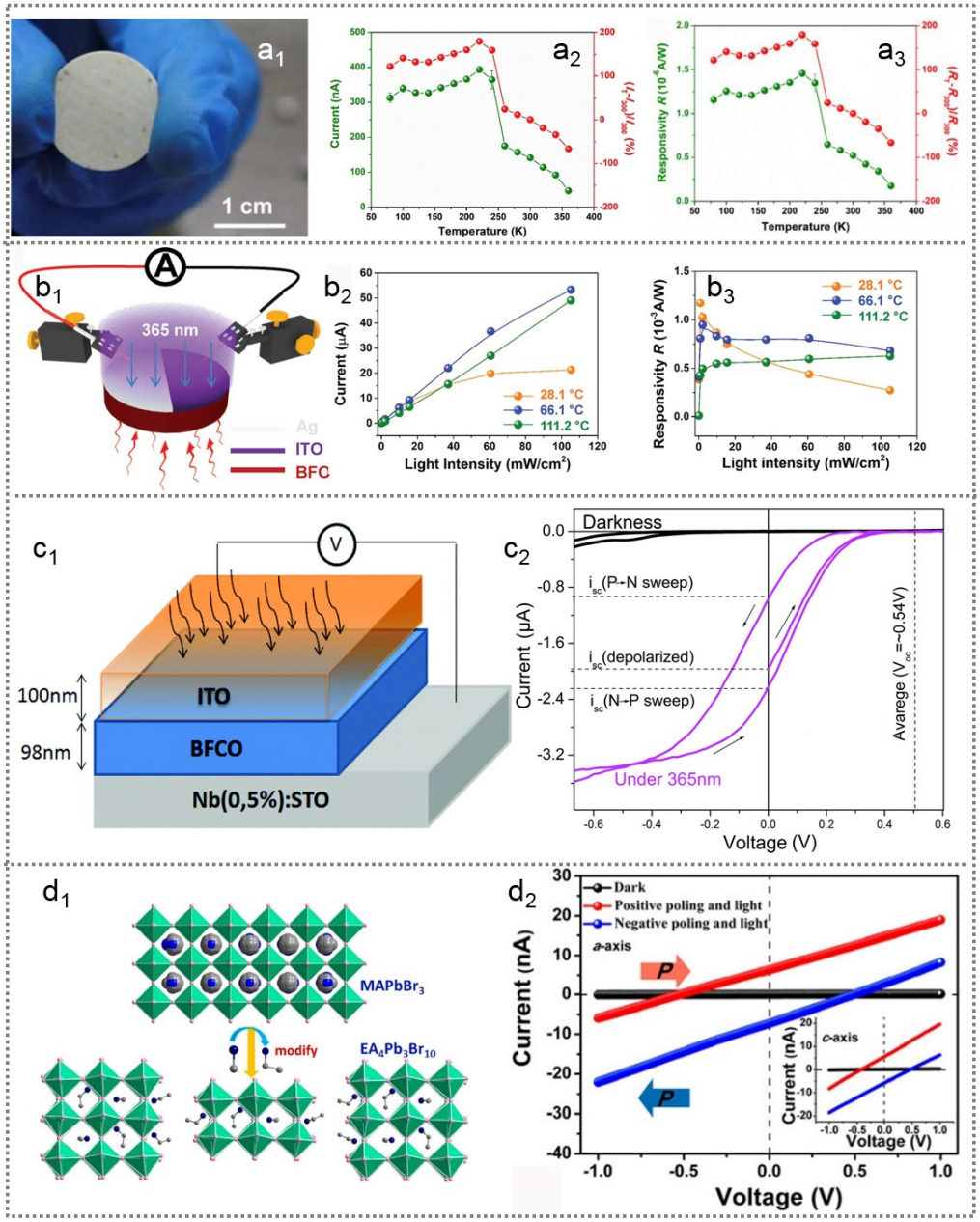

Figure 6. Solar energy scavenging devices. a) ITO/BTO/ITO photodetector, a_1) Image of ITO/BTO/ITO device, a_2) Photocurrent-temperature curve, a_3) Responsivity-temperature curve. Reproduced with permission.[173] Copyright 2019, Elsevier. b) Ag/BFO/ITO UV photo detector, b_1) Schematic of photovoltaic test on Ag/BFO/ITO device, b_2, b_3) Variation of b_2) photocurrent and b_3) responsivity with light intensities at different temperatures. Reproduced with permission.[199] Copyright 2019, Wiley-VCH. c) c_1) Schematic of ITO/BFCO/Nb:STO device, c_2) I-V curve of ITO/BFCO/Nb:STO device. Reproduced with permission. [200] Copyright 2018, Royal Society of Chemistry. d) $EA_4Pb_3Br_{10}$ ferroelectric photovoltaic device, d_1) sketch map for tailoring a 3D pattern of $MAPbBr_3$ into a 2D three-layer $EA_4Pb_3Br_{10}$, d_2) Voltage dependence of

photocurrent curves of $EA_4Pb_3Br_{10}$. Reproduced with permission.[178] Copyright 2019, America Chemical Society.

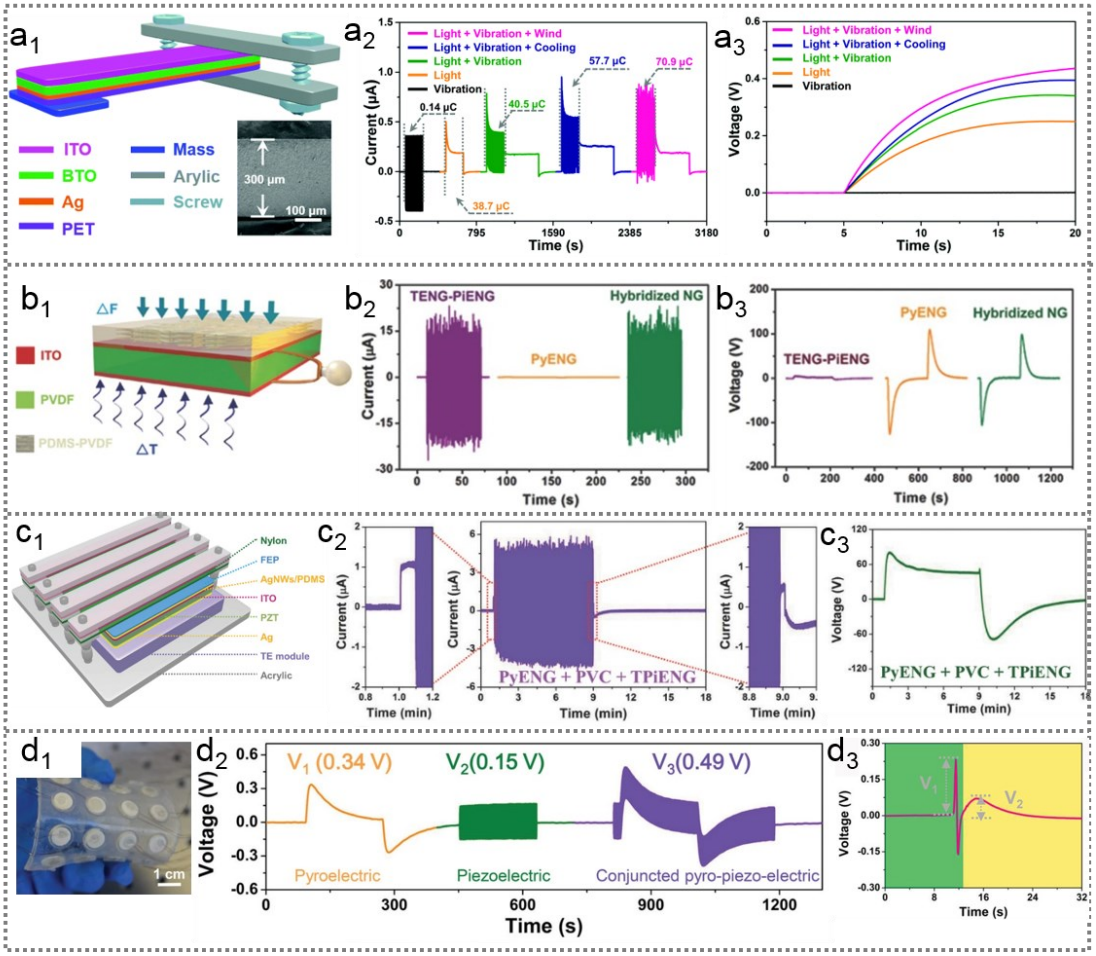

Figure 7. Coupled nanogenerators based on different effects. a) Piezo-pyro-photoelectric effects coupled BTO based nanogenerator, a_1) Schematic of ferroelectric BTO based device., a_2) Output currents, a_3) Charging voltage curves of the device for a 4.7 μF capacitor. Reproduced with permission.[67] Copyright 2019, Royal Society of Chemistry. b) Tribo-Piezo-Pyroelectric effects coupled polymer based nanogenerator, b_1) Schematic of the hybridized nanogenerator, b_2) Output current and b_3) Voltage of the TENG-PiENG, PyENG, and hybridized NG. Reproduced with permission.[179] Copyright 2016, Wiley-VCH. c) Piezo-tribo-pyro-photoelectric effects coupled nanogenerator, c_1) Schematic of one-structure based multi-effects coupled nanogenerator, c_2) Output current and c_3) Voltage of coupled nanogenerator of "PyENG + PVC + TPiENG". Reproduced with permission.[181] Copyright 2016, Wiley-VCH. d) Piezo-pyroelectric effects coupled BTO/PDMS sensor system, d_1) Image of bending 4×4 pyro-piezo-electric sensing substrate, d_2) Output voltage of individual temperature, pressure, and temperature-pressure combined stimulus, d_3) Output voltage as a finger touching sensor. Reproduced with permission.[180] Copyright 2019, Wiley-VCH.

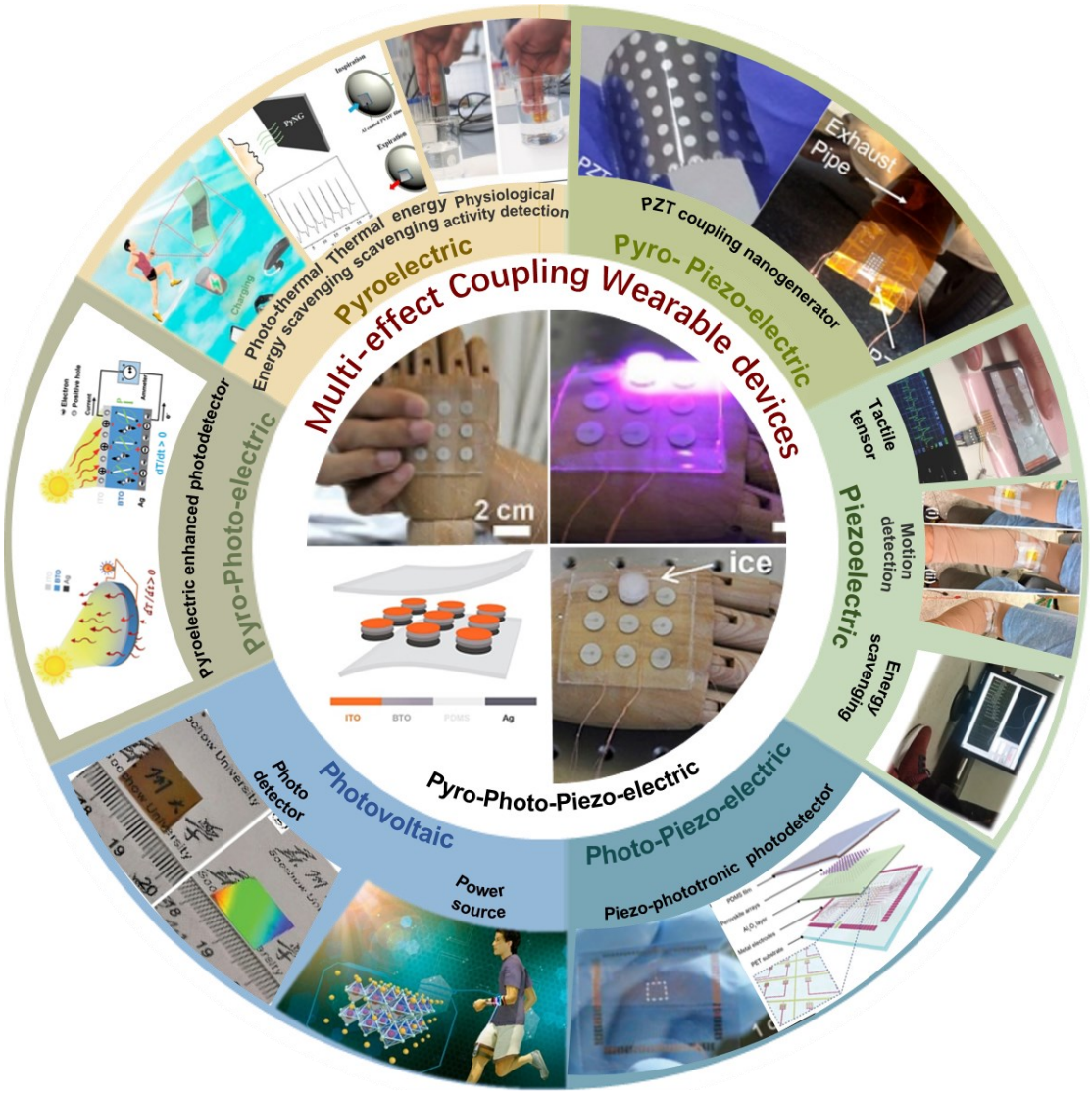

Figure 8. Ferroelectric wearable devices. Reproduced with permission.[185] Copyright 2017, Wiley-VCH. Reproduced with permission.[190] Copyright 2018, Elsevier. Reproduced with permission.[183] Copyright 2020, Elsevier. Reproduced with permission.[184] Copyright 2019, Wiley-VCH. Reproduced with permission.[188] Copyright 2019, Wiley-VCH. Reproduced with permission.[187] Copyright 2019, America Chemical Society. Reproduced with permission.[154] Copyright 2017, Elsevier. Reproduced with permission. [186] Copyright 2020, Elsevier. Reproduced with permission.[195] Copyright 2017, Wiley-VCH. Reproduced with permission.[193] Copyright 2018, Wiley-VCH. Reproduced with permission.[192] Copyright 2017, Wiley-VCH.

Table 1 Piezoelectric Nanogenerators

Material	OC voltage	SC current (density)	Power density	Work Condition	Reference
PZT ceramic foam	65 V	~0.26 nA/cm^2	-	15% stretchable strain	[50]
PZT nano ribbons		250000 nA/cm^2	-	8% periodic stretch strain	[27]
BTO thin films	1 V	190 nA/cm^2	7 mW/cm^3	0.40-0.55% strain	[134]
$BaTiO_3$ nanowire arrays	-	-	0.00627 mW/cm^3	direct vibration excitation at 1g acceleration	[49]
KNN nanorod arrays	0.38 V	18.8 nA/cm^2	101 mW/cm^3	1 kgf of external compressive force	[48]
P(VDF-TrFE)	3.9 V	-	-	air flow speed of 3m/s	[135]
$K_{0.5}Na_{0.5}NbO_3$-$BaTiO_3$/PVDF	160 V	44.4 nA/cm^2	-	0.4 N compressive force	[45]
$GaFeO_3$/PVDF	3.5 V	1.78 nA/cm^2	-	manual finger tapping of device	[133]

OC: open circuit, SC: short circuit

Table 2 Pyroelectric Nanogenerators

Material	OC voltage	SC current	pyroelectric coefficient	energy density	power density	FoM	Work Condition	Reference
PMN-0.32PT thin film	-	~90 nA	−550 μC/m^2 K	1.06 J/cm^3	5.26 ×10^8 μW/cm^3	-	sinusoidal oscillation of temperature with amplitude θ_{FE} = 10 K	[138]
TGS nanorods	-	0.1 nA	167 μC/m^2 K	-	-	F_E=72 J/m^3 K^2, F_v=820 kV/m K	temperature change at 0.5 Hz at 44°C	[47]
Porous PZT ceramics with 20% porosity	15.2 V	-	~320 μC/m^2 K	1653 μJ/cm^3	-	F'_E=9 pm^3/J, F_v=0.03 m^2/C	temperature fluctuations of 1.6 °C s^{-1}	[142]
0.8($Bi_{0.5}Na_{0.5}$)TiO_3-0.2Ba($Bi_{0.5}Nb_{0.5}$)O_3	-	-	~0.5 μC/m^2 K	425 kJ/cm^3	-	-	heating rate of 2 °C min^{-1} at 1 kHz	[157]
$LiTaO_3$ thin films	-	-	31.9±5.0 μC/m^{2}K	-	-	-	known variation of temperature	[153]

$0.97K_{0.5}Na_{0.5}NbO_3$-$0.03Bi_{0.5}Na_{0.5}ZrO_3$	-	-	45446 μC/m^2 K	-	-	F_i=1.83×10^{-9} m/V, F_v=0.17 m^2/C, F_E=5.3 J /m^3 K	ΔT is 0.22 K at 100 °C	[155]
PVDF thin film	42 V	2500 nA	27 μC/m^2 K	-	0.678 μW/cm^2	-	human respiratory at 5 °C	[154]
$PbZr_{0.53}Ti_{0.47}O_3$/ $CoFe_2O_4$ multilayers	-	-	-	47372 kJ m^{-1} cycle^{-1}		-	Olsen cycle	[46]

Table 3 Solar Energy Scavenging Devices

Material	OC voltage	SC current (density)	responsivity	Power	PCE	G	Work Condition	Reference
$BaTiO_3$ ceramics	-	0.1908 $\mu A/cm^2$	-	-		4.46×10^{-6}	220 K, 405 nm illumination 131 mW/cm^2	[173]
$BaTiO_3$ crystal		17000 $\mu A/cm^2$			3.9%		under full AM1.5 G	[164]
$BiFeO_3$ ceramics	~0.5 V	133.8 $\mu A/cm^2$	-	6.48 μW		-	365 nm, 271.4 mW cm^{-2}, 42.5 °C, cooling	[174]
$BiFeO_3$ ceramics	0.6 V	132.1 $\mu A/cm^2$	6.56×10^{-4} A /W	6.74 μW		-	66.1 °C, 365 nm light (105.2 mW/ cm^2)	[51]
$CsPbBr_3$ nanowires	-	-	4400 A/W	-		1.3×10^{-4}	RT, 0.2 mW/cm^2, 405 nm	[175]
$(K_{0.49}Na_{0.49}Ba_{0.02})(Nb_{0.99}Ni_{0.01})O_{2.995}$	0.11 V	0.03 $\mu A/cm^2$	-	~60 μW	0.12%	-	405 nm, 50 mW laser	[172]
$[KNbO_3]_{1-x}[BaNi_{1/2}Nb_{1/2}O_{3-\delta}]_x$	3.5 V	0.04 $\mu A/cm^2$	-	-	>3%	-	illumination by a halogen lamp delivering approx. 4 mW/cm^2	[162]

G: gain, RT: room temperature, PCE: Power Conversion efficiency

The table of contents entry: Energy harvesting materials and devices is a research hotspot for years. Ferroelectric materials with multi-effects play a key role in energy scavenging field. The theories, equations and application of ferroelectric materials for harvesting energy from different energy sources have been summarized in this manuscript.

Keywords: ferroelectric, piezoelectric, pyroelectric, ferroelectric photovoltaic, nanogenerator

Authors: *Hongyu Li, Chris R. Bowen, and Ya Yang**

Title: Scavenging Energy Sources Using Ferroelectric Materials

TOC figure:

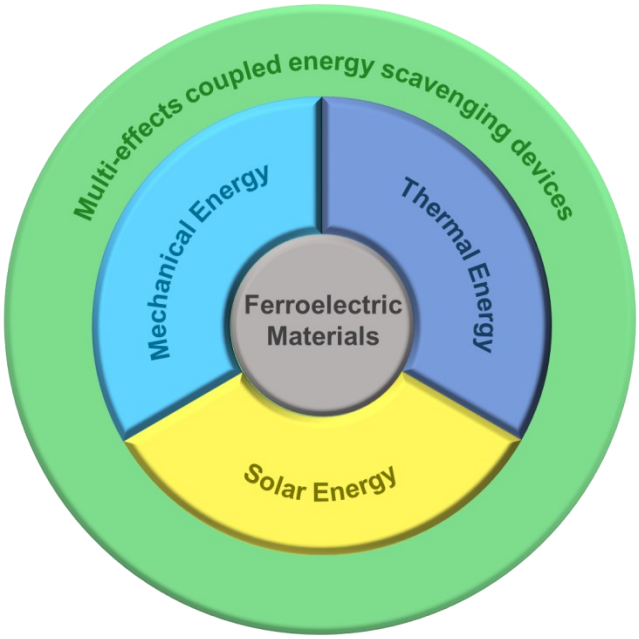

Abstract:

Ferroelectric materials have attracted interest for over a hundred years as a result of their spontaneous polarization and a polarization orientation that can be reversed by the application of an external electric field. In addition, the degree of polarization can be affected by external stimuli such as vibrations, stress, heat and light. These properties enable ferroelectric materials to be used to fabricate nanogenerators, which are devices used in energy scavenging applications and provide an opportunity to obtain electrical energy from a variety of external stimuli. This review discusses the development of ferroelectric based nanogenerators for scavenging mechanical, thermal and solar energies through the piezoelectric effect, pyroelectric effect and photovoltaic effect, respectively. The mechanisms of the effects and the pathways to optimize the output performance of the nanogenerators are analysed in detail. Recent

developments in energy harvesting using ferroelectric materials are discussed with the objective to motivate attention and efforts in this growing field.